EMPIRICAL EVIDENCE FOR THE ASSOCIATION OF THE EL NIÑO-SOUTHERN OSCILLATION WITH TERRESTRIAL VEGETATION DYNAMICS IN THE WESTERN UNITED STATES

Matthew P. Dannenberg

A thesis submitted to the faculty of the University of North Carolina at Chapel Hill in partial fulfillment of the requirements for the degree of Master of Arts in the Department of Geography.

Chapel Hill
2013

Approved by:

Conghe Song

Erika Wise

Aaron Moody

ABSTRACT

MATTHEW P. DANNENBERG: Empirical Evidence for the Association of the El Niño-Southern Oscillation with Terrestrial Vegetation Dynamics in the Western United States (Under the direction of Conghe Song)

Timing of plant life cycle events (phenology) and annual plant productivity represent key interactions between the atmosphere and the biosphere, with implications and feedbacks for climate and ecosystem functions. The El Niño-Southern Oscillation (ENSO) system is the dominant source of interannual climate variability in the western United States, with important effects on temperature, precipitation, and drought. In this study, the connection between ENSO and terrestrial vegetation dynamics is examined using remotely sensed vegetation indices, eddy covariance flux tower observations, ENSO indices, and spatially-resolved climate data. El Niño events are associated with an increase in primary production throughout the western U.S., and with an earlier growing season in much of the Pacific Northwest and parts of the Southwest. The correlation between total annual production and the Southern Oscillation Index is highest in mid- to late-winter prior to the growing season, suggesting some predictive power in advance of the growing season.

ACKNOWLEDGEMENTS

I gratefully acknowledge the support, advice, and patience of my advisor, Conghe Song, who has both challenged and encouraged me over the past two years. I also thank the members of my thesis committee—Erika Wise and Aaron Moody—for their thoughts and comments throughout the research and writing process. I am also deeply indebted to both Taehee Hwang and Josh Gray, both for sharing their experience and insight in remote sensing of land surface phenology and for their comments on the finished manuscript. Thanks also to the members of my research group—Chris Hakkenberg, Qi Zhang, and Yulong Zhang—for their friendship and advice, and for patiently listening to and commenting on my research presentations.

I am especially grateful to my family for their constant, loving support throughout the years, and to my teachers—from Kindergarten through college—for instilling in me a love of learning and a fascination with the world around me. Most of all, this work would not have been possible without the love and support of my wife, Becky.

TABLE OF CONTENTS

LIST OF TABLES

Table

LIST OF FIGURES

Figure

LIST OF ABBREVIATIONS

DOY ..... Day of Year

ENF ..... Evergreen Needleleaf Forest

ENSO ..... El Niño-Southern Oscillation

EOS ..... End of Growing Season

ΔEOS ..... Difference Between El Niño EOS and La Niña EOS

EVI ..... Enhanced Vegetation Index

GPP ..... Gross Primary Production

GRS ..... Grassland

LOS ..... Length of Growing Season

ΔLOS ..... Difference Between El Niño LOS and La Niña LOS

LSP ..... Land Surface Phenology

MF ..... Mixed Forest

MLCD ..... MODIS Land Cover Dynamics

NPP ..... Net Primary Production

ΔNPP ..... Difference Between El Niño NPP and La Niña NPP

ONI ..... Oceanic Niño Index

PFT ..... Plant Functional Type

SHB ..... Shrub Land

SOI ..... Southern Oscillation Index

SOS ..... Start of Growing Season

ΔSOS ..... Difference Between El Niño SOS and La Niña SOS

SST ..... Sea Surface Temperature

CHAPTER 1

INTRODUCTION

Terrestrial vegetation is one of the key links between the biosphere and the atmosphere. Fixation of carbon dioxide through photosynthesis (gross primary production, or GPP) and total plant biomass accumulation (net primary production, or NPP) are among the primary means by which vegetated ecosystems interact with the climate system. GPP and NPP are also the sources of the fundamental resources (food and fiber) required by all biological organisms, including humans [*Running*, 2012]. Timing of plant life cycle events (phenology) is a dominant biological cycle with strong effects and feedbacks both on climate [*Keeling et al.*, 1996; *Peñuelas et al.*, 2009] and on terrestrial ecosystem functions, including evapotranspiration, carbon fixation, and ecosystem respiration [*Morisette et al.*, 2009; *Richardson et al.*, 2010]. Vegetation phenology also affects human health [*Morisette et al.*, 2009], agriculture [*Brown and De Beurs*, 2008], surface meteorology [*Schwartz*, 1992; *Bonan*, 2008a, 2008b; *Richardson et al.*, 2013], trophic interactions [*Chesson et al.*, 2004; *Liu et al.*, 2011], and vegetation community structure, interspecific competition, and success of invasive species [*Willis et al.*, 2008, 2010; *Wolkovich and Cleland*, 2011; *Cleland et al.*, 2012; *Fridley*, 2012].

Both primary production and vegetation phenology are strongly related to climate. Climatic limitations on plant production can include temperature, moisture availability, and incident photosynthetically active radiation. The geographic distribution of climate

limitations to plant growth is not uniform, and multiple factors are often co-limiting to growth [*Nemani et al.*, 2003]. The onsets of leaf emergence, maturity, senescence, and dormancy are also dependent on climate signals [*Körner and Basler*, 2010]. In temperate and high-latitude ecosystems, photosynthetic activity can be triggered by multiple mechanisms, including a physiological chilling requirement to break winter dormancy followed by temperature- and photoperiod-induced leaf emergence [*Archibold*, 1995; *Zhang et al.*, 2007]. In arid and seasonally moist ecoregions, leaf and shoot growth is often triggered by the beginning of the wet season and senescence and leaf abscission by depletion of soil moisture, though photosynthesis may also be limited by low temperatures in cool deserts such as the Great Basin of the western United States [*Archibold*, 1995; *Jolly and Running*, 2004; *Jolly et al.*, 2005].

The El Niño-Southern Oscillation (ENSO)—a recurring 2-7 year cycle of coupled ocean-atmosphere dynamics in the equatorial Pacific—has long been recognized as one of the dominant modes of interannual climate variability, with teleconnections to surface climate across the globe [*Trenberth*, 1997a; *Bonan*, 2008a]. La Niña events occur during periods with a strong Walker circulation and anomalously strong sea surface temperature (SST) gradients across the equatorial Pacific (with higher SST in the western Pacific and lower SST in the eastern Pacific), while El Niño events occur with a weakened Walker circulation and reduced SST gradient in the equatorial Pacific. Temperature and precipitation in the western United States are significantly linked to ENSO, with El Niño (La Niña) events being associated with dry (wet) and warm (cool) anomalies in the Pacific Northwest and with wet (dry) conditions in much of California and the arid Southwest [*Redmond and Koch*, 1991]. The ENSO cycle may also be relatively predictable, with

forecasting lead-times up to one year [*Trenberth*, 1997a], though there are limits to the ability of statistical models accurately predict ENSO [*McPhaden et al.*, 2006]. While recent studies have found that current ENSO strength is anomalously high by historical standards [*Cobb et al.*, 2013], there is considerable uncertainty surrounding the response of ENSO to global climate change, with strong disagreement among scholars over whether the cycle will become more Niño- or Niña-like [*McPhaden et al.*, 2006; *Vecchi et al.*, 2008]. Different "flavors" of El Niño events—resulting from variation in the location of sea surface temperature warming in the central or eastern tropical Pacific—are also associated with different climate impact patterns, and there may be long-term trends towards an increasing frequency of central Pacific El Niño "flavors" [*Yeh et al.*, 2009, 2011; *Newman et al.*, 2011].

Given the strength, short-term predictability, and future uncertainty of the ENSO-climate connection, characterizing the relationship between ENSO and terrestrial vegetation is an important area of research with implications ranging from forecasting agricultural yield to managing natural resources. Previous studies have found that the ENSO cycle is associated with variability in normalized difference vegetation index (NDVI) [*Anyamba et al.*, 2001, 2002; *Buermann et al.*, 2003], primary production [*Behrenfeld et al.*, 2001; *Potter et al.*, 2003a, 2003b, 2004; *Hashimoto et al.*, 2004], and phenology [*Vicente-Serrano et al.*, 2006; *Brown et al.*, 2010; *McCabe et al.*, 2012]. Studies in North America have suggested that overall carbon flux is not significantly related to ENSO, but that there is large regional heterogeneity in the response of NPP to ENSO [*Potter et al.*, 2003a]. Likewise, across the U.S. few individual phenological time-series were significantly related to ENSO, but the continent-wide distribution of ENSO-induced green-up date divergence suggested a closely coupled relationship [*McCabe et al.*, 2012].

Here, the association between ENSO and vegetation dynamics in the western United States (31.1°N – 49.2°N latitude, 108.0°W – 125.2°W longitude) is explored in further detail using ENSO indices, spatially-resolved climate data, eddy covariance flux tower data, and remotely sensed estimates of primary production and phenological events from the MODerate Resolution Imaging Spectroradiometer (MODIS). Since phenological dates are extracted from remotely sensed data, rather than from ground-based canopy observations, satellite-derived phenological estimates are referred to as "land surface phenology" (LSP): the seasonal "greenness" signal aggregated for all objects within a pixel [*Zhang et al.*, 2006; *White et al.*, 2009]. As such, LSP derived in this study is not necessarily indicative of specific plant life cycle events, and all phenological terminology adopted throughout this paper should be interpreted as referring only to the aggregated seasonal greenness trajectory for individual pixels.

The objective of this study is to examine the association between ENSO and two satellite-assessed aspects of vegetation dynamics: LSP and primary production. Since the ENSO cycle has been observed to affect both surface temperature and precipitation in the western United States, and since both plant phenology and productivity are driven by climate, it seems very likely that interannual ENSO variability will be associated with interannual variability in LSP and primary production. Particularly, El Niño-induced increases in early growing season temperature in the Pacific Northwest and precipitation in the arid Southwest seem likely to result in an earlier start of the growing season throughout much of the western United States, which may also result in a longer growing season associated with El Niño events. Primary production in most of this region is co-limited by temperature and water availability [*Nemani et al.*, 2003], and historical ENSO impact

patterns suggest that these climate constraints may be alleviated following El Niño events. It therefore seems likely that El Niño events will be associated with increases in primary production throughout much of the western U.S. Given the importance of vegetation phenology and productivity to both natural and human systems, better understanding of interannual sources of variability could be important for agricultural forecasting, forest and invasive species management, and conservation planning.

CHAPTER 2

DATA AND METHODS

2.1. MODIS Products and Pre-Processing

Monitoring of terrestrial vegetation from space-borne sensors is largely based on the use of spectral vegetation indices (SVI), many of which were developed in the 1970s and 1980s for use with the Landsat MSS and TM sensors [*Tucker*, 1979; *Cohen and Goward*, 2004]. Since the launch of the Advanced Very High Resolution Radiometer (AVHRR) sensor in the early 1980s, SVI from coarse spatial and high temporal resolution satellite sensors have been applied for continental- to global-scale analysis of land cover [*Tucker et al.*, 1985; *Hansen et al.*, 2000; *Loveland et al.*, 2000; *Friedl et al.*, 2002, 2010], primary production [*Potter et al.*, 1993; *Field et al.*, 1995; *Prince and Goward*, 1995; *Running et al.*, 2004], and vegetation phenology [*Justice et al.*, 1985; *Reed et al.*, 1994; *Moulin et al.*, 1997; *White et al.*, 1997; *Zhang et al.*, 2003]. MODIS, launched onboard the EOS-Terra satellite in late 1999, improves upon AVHRR spatial resolution, radiometric response, geolocation, and atmospheric correction, and the MODIS land science team produces and validates many higher level land surface products for use in global change research [*Running et al.*, 1994; *Justice et al.*, 1998]. MODIS-derived datasets used in this study (Table 1) include annual NPP (MOD17A3), 16-day enhanced vegetation index (EVI; MOD13A2), land cover type (MCD12C1), and land cover dynamics (MCD12Q2).

The MOD17 primary production algorithm is based on light-use-efficiency theory, estimating GPP based on an efficiency factor that converts the absorbed photosynthetically active radiation (APAR) [*Running et al.*, 2004]. Daily GPP is then summed to an annual product, and NPP is estimated as the annual sum of daily GPP minus growth respiration and maintenance respiration of leaves, fine roots, and live woody cells. In this study, only NPP is used since it is ecologically meaningful and is a key component of both the global carbon cycle and ecosystem services used by humans [*Running*, 2012]. Since total production varies greatly within and among biomes in the western U.S.—ranging from the high productivity evergreen forests of the Pacific Northwest to the low productivity shrub lands of the desert Southwest—each pixel time-series (separated into El Niño and La Niña samples, Table 2) is converted from standard MOD17A3 units (kg C/m²/year) to standardized Z-scores, defined as the per-pixel difference between the mean ENSO sample NPP (computed separately for El Niño and La Niña samples) and the mean of the full study period NPP, divided by the per-pixel NPP standard deviation in the full study period.

The global 0.05° (latitude by longitude) resolution MCD12C1 land cover product is a spatially-degraded version the 500 meter MCD12Q1 land cover product, produced globally from MODIS reflectance data and a supervised decision tree classifier [*Friedl et al.*, 2002, 2010]. In this study, the International Geosphere-Biosphere Programme classification scheme is aggregated into four plant functional types (PFT): evergreen needleleaf forest (ENF), mixed forest (MF), shrub lands (SHB, including both open and closed shrub lands), and grasslands (GRS). Urban, barren, and water pixels are not used in subsequent analyses since they include minimal vegetation cover. MCD12C1 also includes land cover classes for savannas, evergreen broadleaf forests, deciduous broadleaf forests, and deciduous needleleaf

forests, but they constitute a comparatively small proportion of the study area and are therefore not included in this study. Understanding and forecasting the effects of interannual climate variation on crop production are important applications at the intersection of remote sensing, environmental science, and climatology, but croplands are not included in this study since the human "fingerprint" on the seasonal SVI signal of agricultural lands—through the effects of irrigation, fertilization, and multiple cropping cycles—make them poorly suited to isolating an ENSO signal.

The MODIS land cover dynamics (MLCD) product (MCD12Q2) annually estimates four phenological "turning points" (onsets of greenness, maturity, senescence, and dormancy, each in day of year [DOY] units) as well as maximum, minimum, and integrated EVI parameters. Land surface phenology (LSP) events for a given year are modeled using a piecewise logistic function fit to 24 months of 8-day enhanced vegetation index (EVI) calculated from the MODIS nadir and bidirectional reflectance distribution function (BRDF) adjusted reflectance (NBAR) dataset [*Schaaf et al.*, 2002; *Zhang et al.*, 2003; *Ganguly et al.*, 2010]. The MLCD algorithm produces LSP estimates for up to two annual growth cycles (e.g., in the case of double-cropped agriculture). For use in this study, only one annual growth cycle is assumed. Where two growth curves are found for a given pixel, early season MLCD metrics (onsets of greenness and maturity) are obtained from the first growth cycle, and late season metrics (onsets of senescence and dormancy) are obtained from the second growth cycle, thus reducing the complication of estimating ENSO-LSP relationships for multiple annual growth cycles.

MLCD does not produce phenology estimates for pixels with minimal EVI seasonality or with missing observations near phenological turning points [*Ganguly et al.*,

2010]. In much of the Southwest, where vegetation cover may be sparse, MLCD did not produce LSP estimates during several years between 2001 and 2010 (Figure A1), resulting in two or fewer annual LSP estimates for El Niño and La Niña samples throughout much of the study area (Figure A2). An attempt is made to mitigate this issue and to extend the observational period by producing an additional LSP dataset using MODIS-observed vegetation indices from 2000-2011. Extraction of phenological signals from remotely sensed imagery is very sensitive to missing vegetation index observations, particularly when those missing data are located near transition points [*Zhang et al.*, 2009]. Since the MLCD estimates are produced annually using 8-day resolution NBAR data, a maximum of 46 observations are available for fitting of a seasonal vegetation trajectory. In this study, an alternative approach is performed by combining EVI observations from multiple years in an attempt to provide more information to the phenology curve fitting procedure. However, if the reason that MLCD failed to produce annual estimates in much of the Southwest is related to other sources of error—such as noise from the soil background or to lack of seasonality due to sparse vegetation cover—then it is likely that the multi-year phenology approach will also fail to produce estimates in these arid regions.

The MODIS vegetation index product (MOD13A2) is used to generate LSP estimates to supplement the 2001-2010 MLCD estimates. MOD13A2 provides 16 day composites of both NDVI and EVI at 1 km spatial resolution [*Huete et al.*, 2002]:

$$NDVI = \frac{\rho_{NIR} - \rho_{RED}}{\rho_{NIR} + \rho_{RED}} \quad (1)$$

$$EVI = 2.5 \times \frac{\rho_{NIR} - \rho_{RED}}{\rho_{NIR} + 6 \times \rho_{RED} - 7.5 \times \rho_{BLUE} + 1}, \quad (2)$$

where ρ_{NIR}, ρ_{RED}, and ρ_{BLUE} are atmospherically-corrected surface bidirectional reflectance values in near infrared, red, and blue portions of the electromagnetic (EM) spectrum,

respectively. Since healthy vegetation is highly reflective in NIR but not in red portions of the EM spectrum, NDVI and EVI are both positively correlated to plant biomass, density, and productivity. The addition of blue band reflectance and canopy background adjustments in EVI makes it less sensitive to residual aerosol effects and soil background noise than NDVI [*Huete et al.*, 1997, 2002; *Xiao et al.*, 2003]. NDVI also tends to saturate over high biomass forest sites, whereas EVI maintains some sensitivity [*Huete et al.*, 1997, 2002]. Since the western United States includes broad heterogeneity in canopy density and background conditions—with a high likelihood of signal saturation in productive Northwestern forests and soil background effects in Southwestern shrub lands—EVI is selected for use in this study. Visual comparison of NDVI and EVI time-series at select pixels also suggests that EVI may be more suitable than NDVI for characterization of seasonal vegetation activity across the full range of biomes in the western U.S. (Figure A3). In addition to the vegetation index layer, the MOD13A2 quality assurance (QA) and day of year (DOY) layers are also retained for screening of poor quality observations and fitting of phenological curves, respectively. EVI observations are only retained if they are flagged as "good" (QA=0) or "marginal" (QA=1) quality in the QA layer. Pixels that do not have at least 20 total EVI observations from 2000-2011, or at least 10 total observations during El Niño or La Niña samples (Table 2), are also discarded from further analyses.

All MODIS products were obtained from the Land Processes Distributed Active Archive Center (LP DAAC) Data Pool [http://e4ftl01.cr.usgs.gov/], after which they were mosaicked and reprojected from the native sinusoidal projection to a geographic projection using the MODIS Reprojection Tool (MRT). The MODIS NPP, EVI, and LSP products were resampled from their native resolutions to 0.01° resolution (approximately 1.1 km at the

equator) using the MRT nearest neighbor resampling method. To scale up to the 0.05° resolution of the MODIS land cover product, a simple average of the 0.01° MODIS pixels was taken within a 5x5 window. Missing values within each 5x5 window were ignored unless they made up more than 60% (15 out of 25) of the pixels, in which case the 0.05° pixel received a "no data" label. Since 16-day composited EVI values within a 5x5 window may have been collected during different days of the year, a simple DOY average is also assigned to the 0.05° pixel. To stratify the ENSO-vegetation relationship by land cover type, a single representative land cover class is derived for each 0.05° resolution pixel using the most frequent classification (i.e. the mode) from the 2001-2010 period (Figure 1).

2.2. Climate Variables

Many indices have been developed to characterize aspects of ENSO evolution [*Trenberth*, 1997b; *Trenberth and Stepaniak*, 2001; *Stenseth et al.*, 2003]. Two ENSO-related indices are used in this study: the Oceanic Niño Index (ONI) [http://www.cpc.ncep.noaa.gov/products/analysis_monitoring/ensostuff/ensoyears.shtml] and the Southern Oscillation Index (SOI) [http://www.cpc.ncep.noaa.gov/data/indices/]. ONI is defined as a three month running mean of SST anomalies in the Niño 3.4 region (5°N – 5°S latitude, 120°W – 170°W longitude), where anomalous SST warming in this region of the tropical Pacific is characteristic of El Niño events. SOI is based on the difference between standardized sea level pressures (SLP) at Tahiti and Darwin, Australia, where a strong SLP gradient generally corresponds to warm SST in the western Pacific (characteristic of La Niña events) while a weak SLP gradient corresponds to warm SST in the eastern tropical Pacific (characteristic of El Niño events).

ONI and SOI capture different aspects of the ENSO ocean-atmosphere connection, and they are used for different purposes in this study. For split sample analyses, each year in the study period (2000-2011) is defined as an El Niño, La Niña, or neutral year based on the criterion that any year with five consecutive cool-season ONI periods—beginning with the preceding August through October (ASO) period and ending with February through April (FMA) of the current year—in excess of +0.5°C (-0.5°C) is an El Niño (La Niña) year (Table 2). Any year that fails to meet this criterion is categorized as a neutral ENSO year. For correlation-based analyses, three month running means of SOI are used starting with August through October (ASO) of the previous growing season through ASO of the current growing season, for a total of thirteen 3-month SOI periods. Since ENSO events tend to be most strongly defined in the North American cool-season, it is very likely that terrestrial vegetation dynamics will be most highly correlated with winter SOI composites, and the 13 lagged SOI periods are used to examine this hypothesis.

Surface climate characteristics associated with El Niño and La Niña events during 2000-2011 are examined using monthly estimates of minimum temperature, maximum temperature, and precipitation from the PRISM Climate Group [*Daly et al.*, 2002, 2008]. Standardized anomalies for both El Niño and La Niña events are derived for February through April (FMA), May through July (MJJ), and August through October (ASO). PRISM resolution (2.5 arcmin, approximately 4 km) is comparable to the 0.05° MODIS resolution used in this study.

2.3. Eddy Covariance Flux Towers

Ecosystem process studies have benefitted greatly from an expanding network of eddy covariance flux towers, which measure exchanges of CO_2, water, and energy between the atmosphere and vegetation canopies [*Baldocchi et al.*, 2001; *Baldocchi*, 2003]. Flux sites are distributed throughout a wide variety of biomes, and the AmeriFlux network [http://ameriflux.ornl.gov/] gathers data from many of the sites throughout North America. Daily level 4 flux data were downloaded for six sites in the western U. S. (Figure 1; Table 3): Blodgett Forest [*Goldstein et al.*, 2000], Tonzi Ranch [*Ma et al.*, 2007], and Sky Oaks [*Sims et al.*, 2006b] sites in California, Santa Rita [*Scott et al.*, 2009] and Kendall [*Scott et al.*, 2010] sites in Arizona, and one of the Metolius sites [*Law et al.*, 2004] in Oregon.

While flux towers do not provide the synoptic spatial coverage of remotely sensed data, they do provide frequent measurements of CO_2 exchange and are often used for validation of high-level datasets (such as GPP/NPP and evapotranspiration) derived from remote sensing inputs [e.g. *Heinsch et al.*, 2006; *Turner et al.*, 2006]. In this study, gap-filled daily GPP estimates at each of these six sites are used for two purposes: 1) comparison with EVI time-series and MODIS-derived phenological trajectories, and 2) further examination of ENSO impacts on seasonal timing of photosynthetic activity and total annual productivity. For each flux site, corresponding 0.01° resolution and 0.05° resolution MODIS EVI pixels are determined based on minimum distance to pixel center-points. The size and shape of a flux tower footprint varies among sites (depending on tower height and vegetation type) and through time (due to changing wind speed and direction, among other environmental variables), but is typically smaller than the observational scale of coarse-resolution satellite imagery [*Turner et al.*, 2003]. Since the MODIS pixels used in this study cover up to 30 km²

or more, direct comparison between MODIS EVI time-series and flux tower GPP time-series are complicated by a host of scaling problems. Additionally, while EVI does track seasonal changes in GPP in many ecosystems [*Rahman et al.*, 2005; *Sims et al.*, 2006a, 2008], it is also sensitive to canopy structural properties (e.g. leaf area index). Thus, EVI and GPP time-series at a given location will not necessarily demonstrate the same seasonal dynamics, and this may be particularly true at evergreen sites [*Sims et al.*, 2006a], where there may be little intra-annual variation in canopy structure but significant seasonal changes in GPP when temperatures reach an optimum level during the peak of the growing season . Given these issues, flux tower-derived GPP data are used as a simple and crude validation of MODIS-derived LSP, not as a formal source of "ground truth" data.

2.4. Derivation of Land Surface Phenology

Phenological modeling from remotely sensed SVI is often based on two processing steps: 1) noise-filtering and temporal smoothing of seasonal SVI observations, and 2) extraction of phenological metrics. Noise-filtering, temporal smoothing, and function-fitting approaches include best index slope extraction (BISE) [*Viovy et al.*, 1992; *Moulin et al.*, 1997; *White et al.*, 1997], outlier analysis [e.g. *Hwang et al.*, 2011; *Gray and Song*, 2012], moving average or median smoothing [*Reed et al.*, 1994], asymmetric Gaussian functions [*Jönsson and Eklundh*, 2004], the discrete Fourier transform [*Moody and Johnson*, 2001], and piecewise or difference logistic regression [*Zhang et al.*, 2003; *Fisher et al.*, 2006]. Methods for determination of phenological transition dates (e.g. start-of-season [SOS] or end-of-season [EOS] metrics) include the use of global SVI thresholds (DOY at which SVI first exceeds a pre-determined value) [e.g. *White et al.*, 2009], local thresholds (adaptively-

chosen on a per-pixel basis) [*White et al.*, 1997; *Fisher et al.*, 2006], and turning point detection methods using forward- or backward-looking delayed moving averages [*Reed et al.*, 1994] or derivatives of curvature functions [*Zhang et al.*, 2003]. While global thresholds are the simplest method to implement, they are inappropriate at large spatial scales where vegetation types may have very different seasonal SVI amplitudes [*White et al.*, 2009]. In the western U.S., for example, the minimum EVI of most ENF pixels would likely be higher than the maximum EVI of some SHB pixels. Likewise, global thresholds may not be appropriate for pixels with limited seasonal SVI variability, as would be expected for many ENF and SHB pixels.

In this study, per-pixel seasonal EVI trajectories are derived using a multi-stage EVI filtering and smoothing process, and LSP metrics are defined using local thresholds. Following *Hwang et al.* [2011], a two-step noise filtering approach is utilized prior to seasonal curve fitting. First, EVI observations at each pixel are grouped and arranged by DOY, and a simple outlier analysis is used to identify noisy observations. Outliers are defined as any EVI observation within a 30 day moving window that is greater than 1.5 times the interquartile range (IQR) above the third quartile or less than 1.5 times the IQR below the first quartile. Any point flagged as an outlier is discarded from further analyses. Second, a modified BISE filter is used to identify noisy observations that were not flagged in the outlier analysis.

Filtered EVI values are split into three samples: El Niño years (2003, 2005, 2007, 2010), La Niña years (2000, 2001, 2006, 2008, 2011), and MLCD overlap years (2001-2010). Since the temporal resolution of the EVI product (MOD13A2) is relatively low (one observation every 16 days) and since LSP metrics are sensitive to missing observations near

phenological turning points [*Zhang et al.*, 2009], a curve fitting procedure is performed using the whole of each sample (with EVI observations arranged by DOY) rather than fitting the function to annual EVI observations. A difference logistic function is used to represent the seasonal EVI trajectory at each pixel [*Fisher et al.*, 2006; *Fisher and Mustard*, 2007; *Hwang et al.*, 2011]:

$$y(t) = c \times \left(\frac{1}{1+e^{a+bt}} - \frac{1}{1+e^{a\prime+b\prime t}}\right) + d, \quad (3)$$

Where *a* and *b* are fitting parameters defining the leaf onset period, *a'* and *b'* are fitting parameters defining the senescence period, *c* is the seasonal EVI amplitude (difference between maximum and minimum fitted EVI) of the smoothed time-series, and *d* is the minimum of the smoothed EVI. The difference logistic function is fit for each pixel using iteratively reweighted, non-linear least squares regression. At each iteration, the EVI observations are reweighted based on the residuals from the previous iteration's fitted model:

$$w = \frac{1}{1+|r|}, \quad (4)$$

Where *w* is a vector of fitted weights (theoretically ranging from 0 to 1) and *r* is a vector of normalized residuals, with each vector containing one element per EVI observation [*Holland and Welsch*, 1977].

SOS and EOS estimates are defined for each pixel-sample as the DOY (rounded to the nearest day) where *y(t)* equals the mid-point between the fitted minimum and maximum EVI values [*Fisher et al.*, 2006]. The inflection points of the logistic functions for each half of the growing season were also considered as SOS and EOS estimates, but in cases where the first logistic function did not reach its maximum before the second function began its increase, the inflection points often resulted in non-sensical estimates of SOS or EOS (e.g.

Figure A4). A length of the growing season (LOS) parameter is defined as the difference (in DOY units) between EOS and SOS.

The MLCD product (MCD12Q2) and flux tower GPP data were used to validate the EVI-derived LSP estimates produced in this study. Average 2001-2010 MLCD LSP estimates are derived from a simple average of the annual estimates. Since MLCD provides different seasonal metrics than the SOS and EOS estimates derived in this study, comparable parameters are defined for each pixel as the midpoint between the onsets of greenness and maturity (for SOS) and the midpoint between the onsets of senescence and dormancy (for EOS). Where the MODIS phenology product identified two seasonal growth cycles, EOS was only obtained from the second growth cycle since this would more closely correspond to the single growth cycle assumed in this study.

Flux tower-derived phenology is determined by fitting the difference logistic model to the GPP time-series in a similar manner as with MODIS EVI: flux data is divided into three samples (El Niño, La Niña, and all years) and the model is fit separately to the average daily GPP of each sample. Under the assumption that ground-based GPP observations are not subject to the same sources of noise that are present in remotely sensed EVI observations (i.e. atmospheric aerosols, cloud contamination, soil or snow background reflectance, geolocation inaccuracy, etc.), and thus that all GPP observations represent "valid" measurements, the GPP time-series are not outlier- or BISE-filtered prior to difference logistic curve fitting. For comparison to MODIS-derived phenology, the flux "all years" curve is compared to a fitted EVI curve generated using the same temporal period as the available flux data. The Kendall grassland site, for example, only has L4 data available from

2004-2007, and therefore only MODIS EVI data from 2004-2007 is used for comparison at this site.

2.5. Assessing ENSO-Induced Patterns in Annual NPP and LSP

Differences between El Niño and La Niña impact patterns on vegetation dynamics are mapped for the study area using a simple difference between average El Niño SOS, EOS, or LOS and average La Niña SOS, EOS, or LOS (hereafter, LSP differences are referred to as ΔSOS, ΔEOS, and ΔLOS). Differences between El Niño and La Niña LSP are mapped using the LSP metrics derived in this study and the LSP metrics from the MLCD product. For NPP, split-sample differences are taken both for the raw NPP data (ΔNPP_{raw}) and for the standardized split-sample anomalies (ΔNPP_{std}). To evaluate impacts on specific vegetation types, average LSP and NPP are also compared for each of the four PFTs used in this study. Previous studies on the ENSO-related precipitation dipole in the western U.S. have noted the presence of a narrow "transition zone" between the Pacific Northwest and the arid Southwest during extreme ENSO events [e.g. *Wise*, 2010]. To determine if a coherent latitudinal pattern is also evident in ENSO impact patterns on vegetation dynamics, zonal mean differences for each LSP metric and NPP are calculated at intervals of 0.1° latitude.

Since MODIS NPP is annually-resolved, ENSO effects on primary production were further evaluated by correlation with 3-month running means of SOI. First, total study area NPP was calculated using the original 1 km MODIS annual primary production (MOD17A3) dataset, since the 0.05° pixels vary in surface area as a function of latitude. Since ENSO events are typically strongest and most clearly defined in the Northern Hemisphere winter, it is very likely that SOI composites during this period will be most strongly related to Western

U. S. vegetation dynamics. Therefore, total study period NPP was correlated against each of the 13 SOI composites, and the period of maximum correlation was determined. Average NPP was then calculated for each of the PFTs in the study area, and correlation analysis was performed using the SOI composite period that was most highly correlated with the total study area NPP. Changes in productivity during El Niño and La Niña years are also examined by summing the average daily GPP observations for each ENSO sample, resulting in an average annual GPP estimate for El Niño years and La Niña years at each site. At the Metolius site, the only La Niña year (2006) contained missing GPP values for the first 19 days of January, so the annual GPP estimates for both ENSO samples are based on sums starting from January 20.

Correlations between LSP and SOI are also examined using the annually-resolved MLCD product, though this analysis may be limited by the short MLCD temporal period (2001-2010) and by many missing annual estimates in the Southwest and parts of the Pacific Northwest (Figure A1). Annual averages and standard deviations of SOS, EOS, and LOS were obtained from all pixels within each PFT, and these averages were correlated against February through April (FMA) SOI. The FMA period was selected due to its relatively high correlation with full study area annual averages of each LSP metric.

CHAPTER 3

RESULTS

3.1. Comparison of LSP Estimates to MLCD and Flux Tower GPP

Average LSP derived from the difference logistic function fitted to the grouped 2001-2010 EVI observations generally follows expected spatial patterns (Figure 2 a-c). Earliest SOS is observed in southern California and southwestern Arizona, while the latest SOS is observed in eastern and northern Arizona, at higher latitudes, and along mountain ranges. Earliest EOS occurs in southern California and western Arizona and in eastern Oregon and Washington, while the latest EOS is observed in eastern and northern Arizona and in southern Utah, and along the Pacific coast. Long LOS occurs along the Pacific coast and in northern Arizona and southern Utah, while the shortest LOS is mostly observed in northern parts of the study area (Montana, Idaho, eastern Washington and Oregon, and northern Nevada). Within these broadly-defined patterns, there is a great deal of heterogeneity, particularly with EOS and LOS in the dry regions of Washington, Oregon, and Nevada, where "pockets" of late EOS and long LOS are observed amid a background of earlier EOS and shorter LOS. The model failed to estimate LSP metrics throughout much of the study area (represented by grey pixels in all maps), particularly along the Cascade and Sierra Nevada mountain ranges, in arid southern California and western Arizona, and in central Idaho and western Wyoming.

Comparison of average 2001-2010 LSP derived in this study ($LSP_{predicted}$) to the average LSP derived from the MODIS phenology product ($LSP_{MCD12Q2}$; Figure 2 d-f) demonstrates that the two approaches arrive at similar spatial patterns. Since both products are based on some form of logistic function, this result is not surprising. While spatial patterns appear quite similar, the estimates themselves diverge in particular regions. For SOS, the divergence is most pronounced in eastern Arizona, where $SOS_{predicted}$ is much later than $SOS_{MCD12Q2}$. For EOS estimates, both methods identified similar patterns of spatial heterogeneity in the Great Basin, but $EOS_{predicted}$ tended to generate more extreme values in the late-EOS "pockets." $EOS_{predicted}$ was also much later than $EOS_{MCD12Q2}$ throughout Arizona, western New Mexico, and southern Utah, and was slightly later along the Pacific coast. $LOS_{predicted}$ generally exhibits more extreme values and much more spatial heterogeneity than $LOS_{MCD12Q2}$, and noticeably longer LOS is predicted in northern Arizona, southern Utah, and the Pacific coasts of Washington and Oregon. The more extreme heterogeneity in $LSP_{predicted}$ compared to $LSP_{MCD12Q2}$ could be driven by two possible sources: 1) differences between the two modeling frameworks or 2) the spatial averaging of MLCD performed in this study for scaling to 0.05° resolution pixels.

Pixel-wise comparison of $LSP_{predicted}$ to $LSP_{MCD12Q2}$, stratified by PFT, suggests several patterns and divergences in LSP estimates produced by the two methods (Figure 3). First, SOS and EOS estimates from the two methods are more closely correlated than LOS estimates. Since LOS is estimated as the difference between EOS and SOS, any divergence in SOS and EOS would be propagated in LOS estimates, which likely explains the lower correlation between $LOS_{predicted}$ and $LOS_{MCD12Q2}$ for most PFTs. Second, SOS and EOS estimates from the two methods agree more closely for MF, SHB, and GRS than they do for

ENF. Since pixels dominated by ENF generally exhibit less seasonal variation in EVI than pixels dominated by other PFTs, greater divergence between ENF estimates from the two models should not be particularly surprising. Finally, whereas SOS estimates typically fall along the 1:1 line for most PFTs (with the exception of SHB), the slope is generally greater than one for EOS and LOS estimates. Like the patterns noted in comparison of the LSP maps, this suggests that the difference logistic method used in this study generated a larger range of EOS and LOS estimates than those generated by MCD12Q2.

Comparison of LSP derived from MODIS EVI to LSP derived from flux tower GPP highlights several strengths and weaknesses of the difference logistic model as applied to remotely sensed SVI in this study area (Table 4). At the two ENF sites (Blodgett and Metolius), there is a distinct seasonal GPP curve but much less seasonal variation in 0.05° resolution EVI. The difference logistic function estimates a much earlier SOS and later EOS (and hence a much longer growing season) from GPP than from EVI at the Blodgett site. At Metolius, GPP-derived SOS and EOS are both earlier than EVI-derived SOS and EOS, but LOS estimates are similar since SOS and EOS are offset by nearly the same number of days. At these ENF sites, negligible seasonal EVI variability in the 0.01° pixels resulted in a flat difference logistic curve and failure of the LSP algorithm to extract SOS or EOS estimates. The seasonal EVI trajectory closely matches the GPP trajectory at Kendall and Santa Rita, and estimates of SOS are very similar, though the EVI-derived difference logistic model tends to estimate a later EOS and longer growing season than is observed from flux tower GPP. While the Sky Oaks GPP exhibits a clear seasonality, EVI is relatively stable throughout the year, and the fitted curves clearly differ from the GPP-derived curve. The Sky Oaks site is in southern California, where the difference logistic function failed to

produce LSP solutions for many pixels. While the EVI and GPP curves at Tonzi Ranch exhibit very similar seasonality, substantial variability in 0.05° resolution EVI from November through January resulted in a poorly fit difference logistic curve and prevented estimation of LSP metrics, while the 0.01° resolution EVI resulted in a well-fit seasonal trajectory and well-estimated LSP metrics (though EOS was earlier than GPP-derived EOS). Overall, with the exception of the Sky Oaks site and the two ENF sites, the SOS estimates from EVI are generally well-predicted by the SOS estimates from flux tower GPP, but there seems to be more uncertainty in EOS estimates (Figure 4). One possible explanation for the differences between GPP- and EVI-derived EOS is the reduction of leaf-level photosynthetic capacity in response to declining photoperiod, which has been observed to precede leaf abscission by up to five weeks [*Bauerle et al.*, 2012].

3.2. ENSO-induced variability in LSP and NPP

Differences in timing of SOS between El Niño and La Niña events (ΔSOS) are most pronounced and coherent in the northern part of the study area and in eastern Arizona and western New Mexico, where there is a general advance in the timing of spring by up to two weeks or more for El Niño years relative to La Niña years (Figures 5a and A5a). Spatial patterns of ΔSOS south of Oregon and Idaho are more heterogeneous and are complicated by large areas of missing values in California and western Arizona. ΔEOS patterns are most pronounced in southern Nevada and Utah and (for MLCD) in southern California and western Arizona, where there is a delay of senescence by two weeks or more for El Niño years relative to La Niña years. Both LSP products identify earlier EOS in eastern Montana during El Niño events (relative to La Niña events) by 20 days or more, and the MLCD

product also identifies much earlier El Niño EOS in eastern Oregon and Washington (Figures 5b and A5b). The spatial manifestation of ΔLOS is particularly heterogeneous with some disagreement between the two LSP products (Figures 5c and A5c), where LSP derived in this study identifies a lengthening of the growing season in El Niño years relative to La Niña years throughout most of the study area while MLCD identifies a longer El Niño growing season throughout the Southwest but little difference in more northern regions.

Distributions of per-pixel SOS, EOS, and LOS stratified by PFT suggest small shifts in phenological timing between El Niño and La Niña events (Figure 6; Tables 5 & 6). There is a great deal of within-class variability in LSP, particularly within SHB, which has a distinctly bimodal distribution for all three LSP metrics (not shown) and relatively wide, flat probability density functions (PDFs) for all three ΔLSP metrics. On average, MF and SHB pixels experience an earlier start to the growing season during El Niño events compared to La Niña events, while (on average) there is very little difference for ENF and GRS. However, for ENF, MF, and GRS, more than two-thirds of pixels experienced an earlier SOS during El Niño events (relatively to La Niña events), while SHB pixels were evenly split between earlier SOS and delayed SOS during El Niño events. With the exception of a slight delay in El Niño EOS for SHB pixels and a small advance for MF pixels, on average there appears to be very little consistent effect of ENSO on EOS within the study area. An advanced SOS for most PFTs and delayed EOS for SHB combine for an average extension of growing season length in El Niño years compared to La Niña years (particularly for SHB, with an average two week extension of LOS). Longer growing seasons during El Niño years were estimated for a majority of pixels (~60%) within each PFT.

Throughout the study area, MODIS-derived NPP is higher during El Niño events than during La Niña events, particularly along the Pacific coast and in Montana, with estimated differences in excess of 100 gC/m²/year for some pixels (Figure 7). Differences in standardized NPP anomalies between El Niño and La Niña events (ΔNPP_{std}) highlights ENSO-related differences in these same regions, but also reveals large differences between ENSO events in many lower productivity regions, where the absolute difference in NPP may be relatively small but where the difference relative to natural variability can be quite large (Figure 8). This includes large areas of Wyoming, western and northern Arizona, and southern California, as well as more isolated pockets of Utah and southern Idaho. Regions with higher productivity during La Niña events make up a very small proportion of the western U. S., and are mostly concentrated in small pockets throughout the Great Basin.

Distributions of per-pixel NPP reveal higher average productivity during El Niño events for all PFTs (Figure 9; Tables 5 & 6). As with LSP, NPP is highly variable within classes. PDFs of ΔNPP_{raw} and ΔNPP_{std} are both centered at values greater than zero, indicating greater average productivity during El Niño years than during La Niña years. The distinction is particularly great for SHB, where (on average) El Niño events are associated with nearly half a standard deviation increase in NPP above the study period mean, while La Niña events are generally associated with slightly below average production. The proportion of pixels within each PFT with greater NPP during El Niño years than during La Niña years ranges from 82% (for ENF) to 92% (for MF).

Total annual study area NPP is negatively correlated with the SOI over most 3-month composite periods, particularly pre-growing season SOI composites, with greater than 90% significance during the winter (Figures 10 and 11). The strongest correlation occurred during

the JFM period ($r = -0.6$, $p < 0.1$), though DJF and FMA periods were also correlated at greater than a 90% significance level. Total NPP varied from about 700 TgC/year during the most extreme positive JFM-SOI (La Niña) year to nearly 850 TgC/year during one of the most extreme negative JFM-SOI (El Niño) years. Average NPP of each PFT was also negatively correlated with JFM-SOI during the study period (Figure 12), with Pearson correlation coefficients ranging from -0.45 for ENF ($p>0.1$) to -0.68 for GRS ($p<0.05$).

With a few exceptions, average LSP metrics for each PFT are not significantly correlated with FMA-SOI, at least partly due to the small number of annual observations (10) available from MLCD. There is also a large amount of within-class variability in LSP for each year, particularly for SHB. For each PFT, SOS is positively correlated with FMA-SOI, suggesting an earlier SOS during El Niño years and later SOS during La Niña years (Figure A6). Relatively high positive correlations between EOS and FMA-SOI are observed for MF ($r = 0.48$; $p > 0.1$) and GRS ($r = 0.58$; $p < 0.1$) (Figure A7). Average LOS is strongly correlated with FMA-SOI only for SHB ($r = -0.76$; $p < 0.05$), indicating a longer growing season during El Niño years than during La Niña years (Figure A8).

There are some distinct zonal differences in LSP and NPP between El Niño and La Niña years (Figure 13). At low latitudes (< 34°), there is a general trend towards earlier spring greening during El Niño events (i.e. negative ΔSOS), though most of this difference is from extreme negative ΔSOS in eastern Arizona and western New Mexico, while the difference logistic function failed to arrive at LSP solutions for many pixels in the Southwest. There is also a less extreme (but more spatially cohesive) trend north of 44^0 toward earlier spring greening during El Niño events. Differences in EOS between El Niño and La Niña are most extreme south of 40^0N, where there tends to be a delay in fall senescence of up to

30 days during El Niño years (i.e. positive ΔEOS), though the magnitude of the difference varies between LSP derived in this study and LSP derived from MLCD. ΔLOS tends to be positive (i.e. longer El Niño growing season) between 31^0N and 34^0N (driven primarily by negative ΔSOS) and between 36^0N and 40^0N (driven primarily by positive ΔEOS), but the two sources of LSP estimates vary in the magnitude of the difference. The small trends toward earlier SOS and earlier EOS in the northern part of the study area during El Niño events tend to result in neutral ΔLOS above 42° latitude, with close agreement between the two sources of LSP estimates.

Differences in standardized NPP anomalies between El Niño and La Niña are greatest between 32^0N and 36^0N and north of 47^0N, where El Niño NPP may be greater than La Niña NPP by up to 1 standard deviation. In fact, zonal ΔNPP is never less than zero, indicating that productivity in El Niño years is consistently higher than that in La Niña years throughout the western U. S. Surprisingly, the zonal NPP differences exhibit very different patterns from zonal ΔLOS. Despite the hypothesis that changes in growing season length would be highly coupled to changes in NPP, the peak difference between El Niño and La Niña LOS occurs in latitudinal bands from about 31°-33° and from about 36°-39°, while differences in NPP peak around 32°-36° and from 47°-49°.

ENSO-related differences in phenology and productivity vary among the six flux sites (Figure 14; Table 7). At Blodgett, Metolius, and Santa Rita, there is little difference in seasonal GPP trajectory between the El Niño (2003, 2005, 2007) and La Niña (2000, 2001, 2006) samples. At Kendall, photosynthetic activity started and ended earlier (on average) during the El Niño years (2005 and 2007) than during the La Niña year (2006). At the Sky Oaks site, productivity was higher throughout 2005 (an El Niño year) than it was during the

2006 (a La Niña year), but the difference logistic model identified earlier SOS, later EOS, and longer LOS during the La Niña year. At the Tonzi Ranch site, the difference logistic function identified a longer growing season and higher peak productivity during the El Niño years (2003, 2005, and 2007), but it did not converge to the typical "smooth" growth trajectory for the La Niña years (2001 and 2006), resulting in a later SOS estimate than if the curve followed the more typical green-up trajectory. At each site, annual GPP was higher (on average) during El Niño years than during La Niña years, particularly at Metolius, Sky Oaks, and Tonzi Ranch. However, the association of ENSO with annual GPP is not necessarily consistent from year to year (Figure A9). At Blodgett, for example, annual GPP was quite high in 2005 but low in 2003 (both El Niño years) while GPP was also high in 2006 and 2001 but low in 2000 (all La Niña years).

CHAPTER 4

DISCUSSION

Comparison of the MODIS-derived LSP metrics from the difference logistic function to LSP metrics from the MODIS land cover dynamics product suggests that the method used in this study is capable of replicating results produced from well-validated studies. The close correlation between these methods is not surprising, however, since they are closely related, with a few main differences. First, in this study, a difference logistic function is used instead of a piecewise logistic function. With the difference logistic method, the two halves of a seasonal growth curve are constrained to be continuous (i.e. to "meet in the middle"), whereas the piecewise function can produce discontinuous growth curves. Second, the MODIS phenology product is estimated annually, whereas LSP estimates in this study are produced by grouping EVI data from multiple years in order to fit an "average" seasonal trajectory for El Niño and La Niña samples. Finally, the extraction of LSP metrics is based on different criteria in the two methods. In this study, SOS and EOS are extracted based on a half-amplitude criterion, where SOS is the mid-point between the minimum and maximum of the fitted EVI curve in the green-up phase, while EOS is the mid-point between the minimum and maximum of the fitted EVI curve in the senescence phase. The MODIS phenology product, on the other hand, estimates four phenological "turning points" as the local maxima and minima of the first derivative of the curvature function [*Zhang et al.*, 2003].

As noted in previous studies, estimation of LSP metrics in arid regions and in areas dominated by evergreen vegetation is complicated by sparse vegetation cover and negligible seasonal SVI variation, respectively [*Zhang et al.*, 2006]. As demonstrated in spatial LSP patterns and in comparison of EVI-derived LSP to flux tower-derived LSP, similar problems are observed in this study. While some of these issues may be primarily related to the SVI signal, there may also be issues related to the curve-fitting procedure or to the LSP metric extraction method. The difference logistic function used in this study may be most appropriate for temperate deciduous forests, where the seasonal growth trajectory is well-defined and where the green-up function typically reaches its maximum before the senescence function begins to influence the shape of the curve. In semi-arid or evergreen vegetation, the method may be less well-suited, as the two logistic functions may be more likely to influence the curve simultaneously, which can result in unrealistically-shaped growth curves and poor estimation of LSP metrics. This can be particularly problematic when estimating LSP metrics from the inflection points of the individual logistic functions, since these points could be on the wrong side of the curve (Figure A4). Use of the mid-amplitude of the fitted EVI curve mitigates the problem of unrealistic SOS and EOS estimates, but the issue is not entirely eliminated (see EVI-derived LSP estimates at Sky Oaks, Table 4).

Shifts in photosynthetic timing and total productivity tend to follow expected spatial patterns based on knowledge of ENSO climate impacts. February through April temperatures (both minimum and maximum) in the Pacific Northwest—where both onset of the growing season and NPP are largely temperature-dependent—tend to be higher during El Niño events than during La Niña events (Figure 15 a-d). As expected, this region

experienced a relatively cohesive shift towards earlier spring growth and higher productivity. Winter precipitation is also considerably higher in the Southwest during El Niño events than during La Niña events (Figure 15 e & f). While greater water availability in February through April may be expected to advance the growing season for arid and semi-arid shrub lands, the ΔSOS spatial pattern is quite heterogeneous in much of the Southwest, though both LSP sources tend to agree that eastern Arizona and western New Mexico exhibit much earlier SOS during El Niño events. This heterogeneity may reflect interacting limitations of water availability and winter temperature, where average maximum temperature is generally cooler during El Niño events in the Southwest (Figure 15 c & d).

Response of EOS to El Niño events may be related to ENSO-climate impact patterns in both the cool-season (FMA) and warm-season (MJJ and ASO), though ENSO climate impact patterns are generally weaker and less spatially cohesive in summer than in winter (Figures 16 and 17). Increased precipitation in the Southwest during the winter months of El Niño years may recharge and delay draw-down of soil moisture, allowing for later EOS in this region, and an extensive region of delayed EOS in southern Nevada and southern California also coincides with increased ASO precipitation during El Niño years. The slightly advanced El Niño EOS observed throughout parts of the Northwest, particularly in eastern Montana, may be related to earlier draw-down of soil moisture due to an earlier SOS. The overall lengthening of the growing season observed throughout much of the western U. S. (particularly the Southwest) during El Niño events likely reflects the combination of warmer winter temperatures throughout the Pacific Northwest and greater moisture availability in the Southwest during winter and in parts of the Southwest during summer months (MJJ and ASO).

Findings from this study may be particularly relevant for short-term forecasting and for better understanding of continental scale responses of vegetation to interannual sources of climate variability. The high correlation of phenology and productivity metrics with winter ENSO indices suggests that some knowledge of both surface climate and vegetation dynamics can be obtained in winter months prior to the growing season. This may be particularly relevant for management of agriculture, wildfire, and invasive species, the latter of which increasingly relies on knowledge of plant phenology [*Wolkovich and Cleland*, 2011]. Knowledge of phenological and productivity responses to climate variability at a broad scale could also be useful for careful targeting of fine scale observations and experiments. While the connection between early season phenology and climate have been well-studied, particularly in temperature deciduous and boreal forests, climatic controls of senescence and dormancy are more poorly understood [*Richardson et al.*, 2013]. The inclusion of both EOS and non-forest, water-limited regions in this study could therefore move in the direction of filling this knowledge gap.

Despite these implications, there are significant limitations in this study. First, the choice of LSP modeling framework could have a large effect on the results of the study. A recent study comparing many commonly-used methods for extracting phenological signals and metrics from remotely sensed SVI found that the methods varied by as much as 60 days in SOS estimates [*White et al.*, 2009]. Therefore, the choice of a different method could alter the relationship observed between LSP metrics and ENSO. Limitations in the ability of the MODIS primary production product to capture seasonal variation in water stress have also been identified in some arid regions, resulting in overestimates of productivity [*Mu et al.*, 2007]. Uncertainty in the MODIS NPP estimates could influence the results of this study,

though this may be slightly mitigated by the primary reliance of this study's results on the ability of MODIS NPP to capture interannual dynamics rather than absolute accuracy.

Arguably the most significant limitation of the study is the relatively short operational period of the MODIS sensor. In particular, it is very likely that the 2000-2011 period only captures a limited range of ENSO variability. There is a great deal of internal variability in the ENSO cycle, and climate impact patterns may not be consistent among all ENSO events with similar SOI or ONI values. Within the MLCD record, there is considerable spatial variability in LSP among particular types of ENSO events. Among El Niño years, for example, 2007 was characterized by earlier than normal SOS throughout the western U.S., while 2010 experienced later than normal SOS in most of the region (Figure A10). Based on peak SOI, these two years were similarly strong El Niño events, though the timing and duration of peak SOI differed from August through October (2007) to December through March (2010). 2005 and 2010 were similar in both peak and timing of SOI, yet spatial LSP patterns also differed substantially between these two years. Similar differences are observed among La Niña years (Figure A11) and neutral years (Figure A12). Thus, while on average there may be an association between interannual variation of vegetation phenology and the ENSO system, the patterns are not necessarily consistent from year to year.

Some of this variation may be related to the location of tropical Pacific sea surface temperature warming, where impact patterns associated with central Pacific warming may be different from those associated with eastern Pacific warming [*Trenberth and Stepaniak*, 2001; *Yeh et al.*, 2009, 2011; *Newman et al.*, 2011]. Additionally, variation in ENSO impact patterns may reflect interactions with multidecadal sources of climate variability, including the Pacific Decadal Oscillation and the Atlantic Multidecadal Oscillation [*Wise*, 2010]. It

seems very likely, therefore, that the 12 year MODIS record only captures a small range of ENSO variability, and that associations between vegetation dynamics and El Niño/La Niña events may exhibit a greater range of variability than indicated in this study. This issue could be mitigated with use of vegetation indices derived from longer satellite records, such as the AVHRR-GIMMS NDVI dataset, but these satellite sensors are also limited by comparatively poor calibration, geolocation, and radiometric response over terrestrial surfaces.

CHAPTER 5

CONCLUSIONS

The response of vegetation dynamics to the El Niño-Southern Oscillation was examined in the western United States using vegetation indices from the MODIS sensor, in addition to ENSO indices, daily GPP estimates from six eddy covariance flux towers, and spatially-resolved temperature and precipitation data from the PRISM Climate Group. Land surface phenology estimates were derived from 16-day time-series of the enhanced vegetation index (using a difference logistic function) and from the MODIS Land Cover Dynamics product. Average seasonal trajectories of EVI generally agreed with flux tower observed GPP at sites with reasonably strong seasonal EVI variation, but LSP metrics (particularly EOS) derived from EVI often differed from LSP metrics derived from the daily GPP. Start of growing season metrics were found to advance by more than a week throughout much of the Northwest during El Niño events, while the response was often stronger but more spatially heterogeneous in the Southwest. ENSO-related changes in end of growing season metrics were most pronounced in the southern regions of the study area (south of 40^0N latitude), which may be associated with reduced water availability during La Niña events. Growing season length was generally longer throughout most of the western U.S. during El Niño events, though with a great deal of variability and heterogeneity. Net primary production was considerably and significantly higher during El Niño than during La Niña events throughout the study area. The peak correlation between total annual NPP and

SOI occurred during the January through March SOI composite period, suggesting some potential for short-term forecasting of vegetation dynamics using ENSO-related indices.

TABLES

Table 1. MODIS products and derived variables used in this study

Product	Units	Resolution	Temporal Period	Citations
MOD17A3 (Primary Productivity)	kgC/m²/year	1000 m	Annual	Running *et al.* [2004]
Net Primary Production (NPP)			(2000-2010)	
MOD13A2 (Vegetation Index)		1000 m	16-day	Huete *et al.* [2002]
Enhanced Vegetation Index (EVI)			(2000-2011)	
MCD12C1 (Land Cover Type)		0.05^0	Annual	Friedl *et al.* [2002,
Evergreen Needleleaf Forest (ENF)			(2001-2010)	2010]
Mixed Forest (MF)				
Shrubland (SHB)				
Grassland (GRS)				
MCD12Q2 (Land Cover Dynamics)	DOY	500 m	Annual	Zhang *et al.* [2003],
Onset of Greenness			(2001-2010)	Ganguly *et al.* [2010]
Onset of Maturity				
Onset of Senescence				
Onset of Dormancy				

Table 2. ENSO years during the study period (2000-2011)

ENSO condition	Number of observations	Years
Neutral	3	2002, 2004, 2009
El Niño[1]	4	2003, 2005, 2007, 2010
La Niña[2]	5	2000, 2001, 2006, 2008, 2011

[1] Five consecutive ONI (in the winter prior to the growing season) greater than 0.5^0C
[2] Five consecutive ONI (in the winter prior to the growing season) less than -0.5^0C

Table 3. Level 4 eddy covariance flux tower data used in this study

Name	Latitude	Longitude	PFT	Years	Principal Investigator
Blodgett Forest	38.8952	-120.9519	ENF	1999-2006	A. H. Goldstein
Kendall Grassland	31.7365	-109.9419	GRS	2004-2007	R. Scott
Metolius Intermediate Pine	44.4523	-121.5574	ENF	2002, 2004-2007	B. E. Law
Santa Rita Mesquite Savanna	31.8214	-110.8661	SVN	2004-2006	R. Scott
Sky Oaks New	33.3844	-116.6403	SHB	2004-2006	W. C. Oechel
Tonzi Ranch	38.4316	-120.9660	SVN	2001-2007	D. D. Baldocchi

Table 4. Comparison of LSP derived from flux tower GPP and from MODIS EVI

	SOS (DOY)			EOS (DOY)		
Name	Flux	0.01^0 EVI	0.05^0 EVI	Flux	0.01^0 EVI	0.05^0 EVI
Blodgett	89		141	280		251
Kendall	211	212	210	261	283	286
Metolius	98		127	259		304
Santa Rita	214	219	215	269	297	295
Sky Oaks	96	40	17	172	365	365
Tonzi	73	64		173	145	

Table 5. Comparison of average LSP and NPP during El Niño and La Niña years (with one standard deviation)

	SOS (DOY)		EOS (DOY)		LOS (DOY)		NPP_{raw} (gC/m²/yr)		NPP_{std}	
PFT	El Niño	La Niña	El Niño	La Niña	El Niño	La Niña	El Niño	La Niña	El Niño	La Niña
ENF	124±29	126±34	256±26	255±25	132±42	129±46	627±217	609±212	0.15±0.25	-0.31±0.28
MF	119±14	125±18	258±20	260±19	139±21	135±23	851±199	827±200	0.26±0.24	-0.28±0.30
SHB	107±51	115±54	255±64	248±60	148±67	133±59	170±122	156±115	0.43±0.20	-0.10±0.26
GRS	115±25	116±28	225±39	225±40	110±39	109±45	209±97	196±93	0.31±0.32	-0.27±0.34

Table 6. Proportion of PFT pixels with El Niño-La Niña differences less than (greater than) 0.

PFT	ΔSOS	ΔEOS	ΔLOS	ΔNPP
ENF	0.67 (0.31)	0.50 (0.46)	0.38 (0.60)	0.18 (0.82)
MF	0.89 (0.09)	0.62 (0.33)	0.35 (0.62)	0.08 (0.92)
SHB	0.48 (0.50)	0.37 (0.61)	0.39 (0.60)	0.11 (0.89)
GRS	0.67 (0.29)	0.51 (0.45)	0.40 (0.57)	0.15 (0.85)

Table 7. Comparison of average LSP and annual GPP during El Niño and La Niña years

	SOS (DOY)		EOS (DOY)		LOS (DOY)		GPP (gC/m²/yr)	
Name	El Niño	La Niña	El Niño	La Niña	El Niño	La Niña	El Niño	La Niña
Blodgett	80	91	303	277	223	186	1261	1209
Kendall	210	232	241	269	31	37	206	187
Metolius[1]	95	100	247	285	152	185	1443	1186
Santa Rita	222	213	272	276	50	63	296	235
Sky Oaks	111	50	186	210	75	160	479	196
Tonzi	71	104	171	162	100	58	924	726

[1] The only La Niña year (2006) had missing GPP values for DOY 1-19, so both GPP sums include only DOY 20+

FIGURES

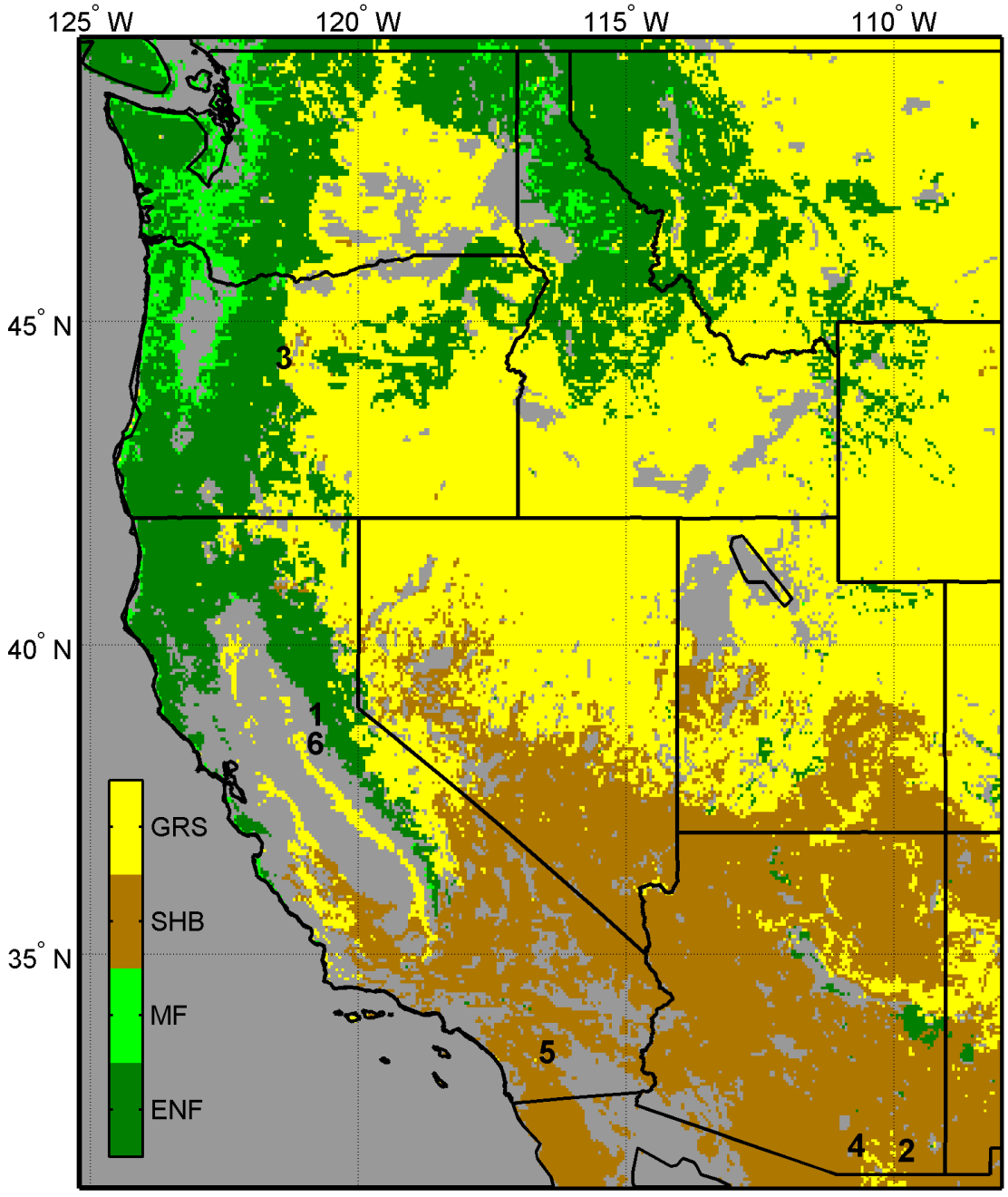

Figure 1: Typical plant functional types in the western United States during 2001-2010, and eddy covariance flux towers used in this study (1: Blodgett, 2: Kendall, 3: Metolius, 4: Santa Rita, 5: Sky Oaks, 6: Tonzi Ranch).

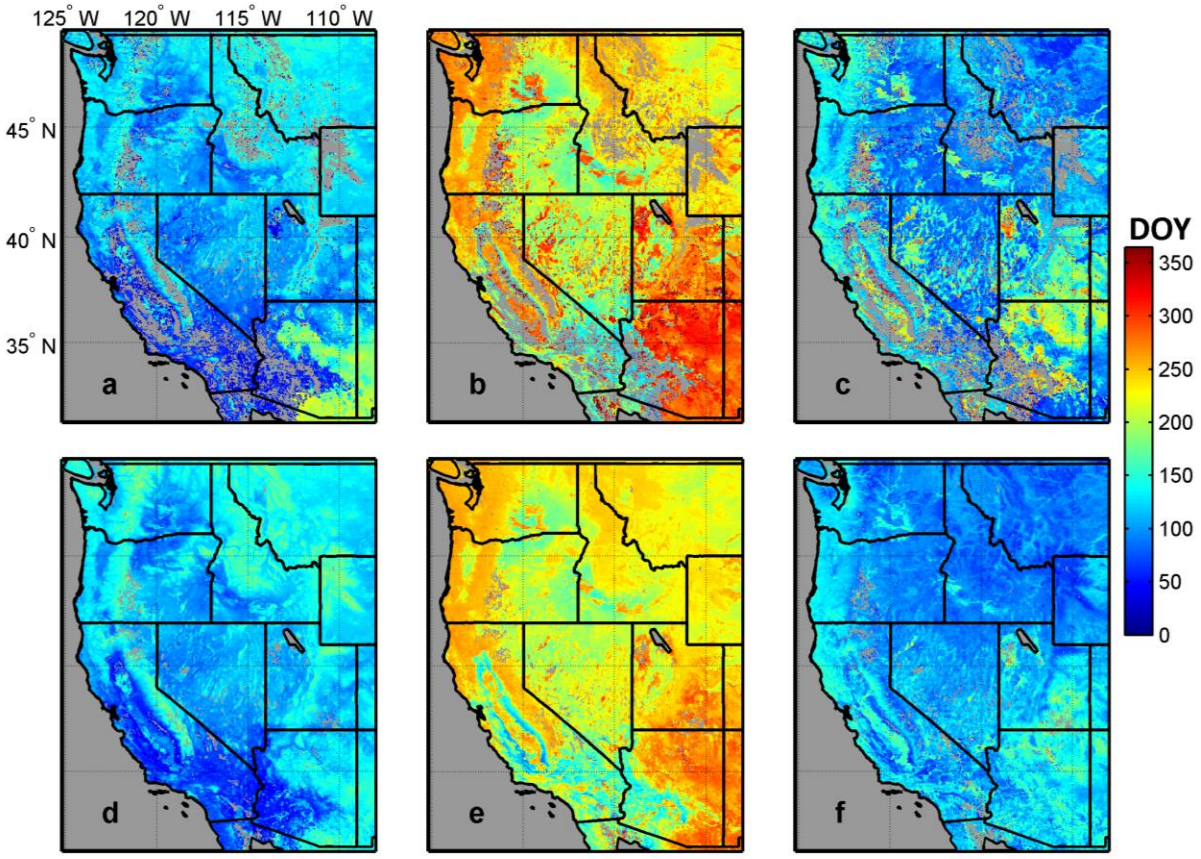

Figure 2: Average 2001-2010 SOS, EOS, and LOS derived from this study (a-c, respectively) and from MLCD (d-f, respectively).

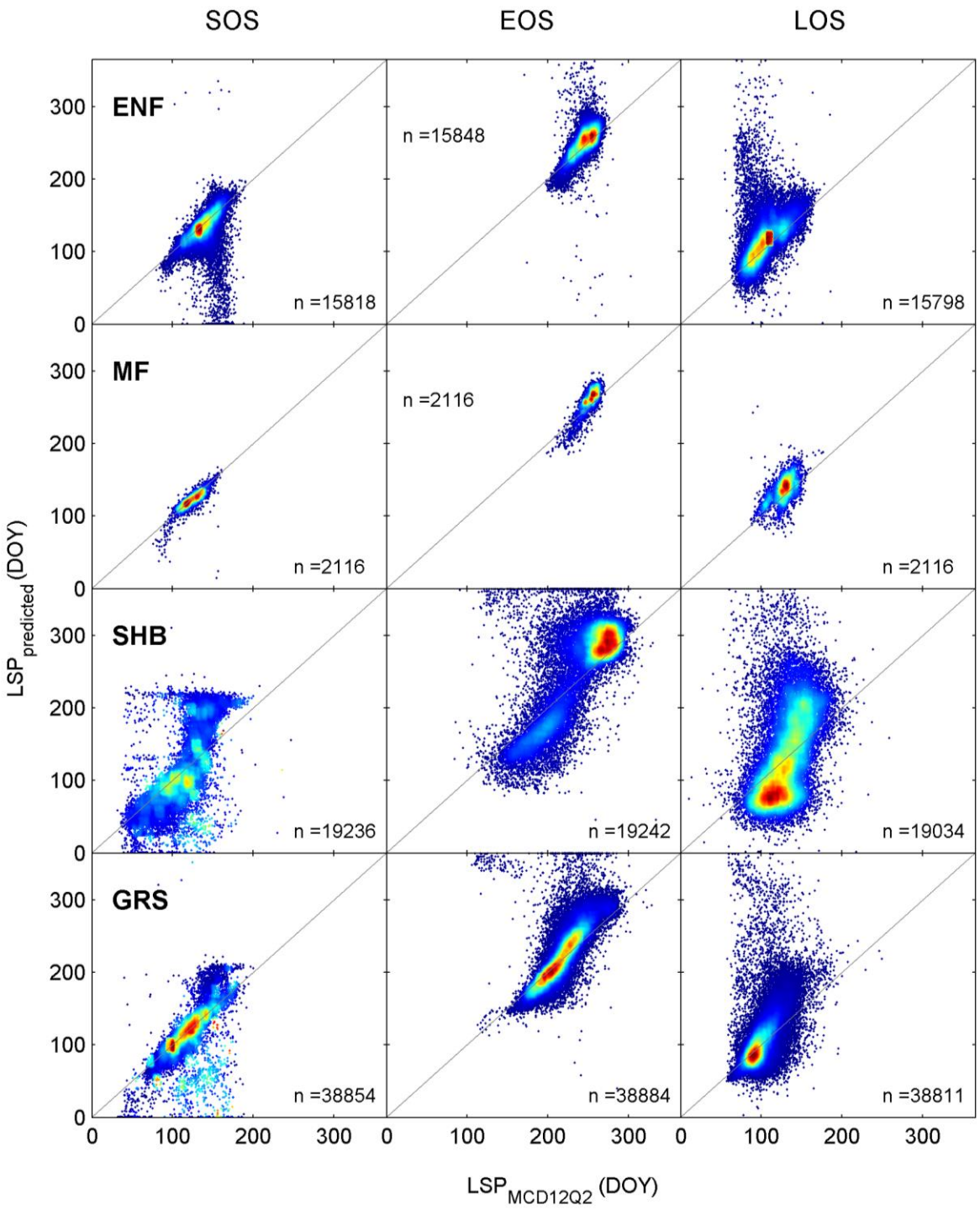

Figure 3: Comparison (by PFT) of average 2001-2010 SOS, EOS, and LOS derived from this study ($LSP_{predicted}$) and from MLCD ($LSP_{MCD12Q2}$). Warm colors indicate high point density.

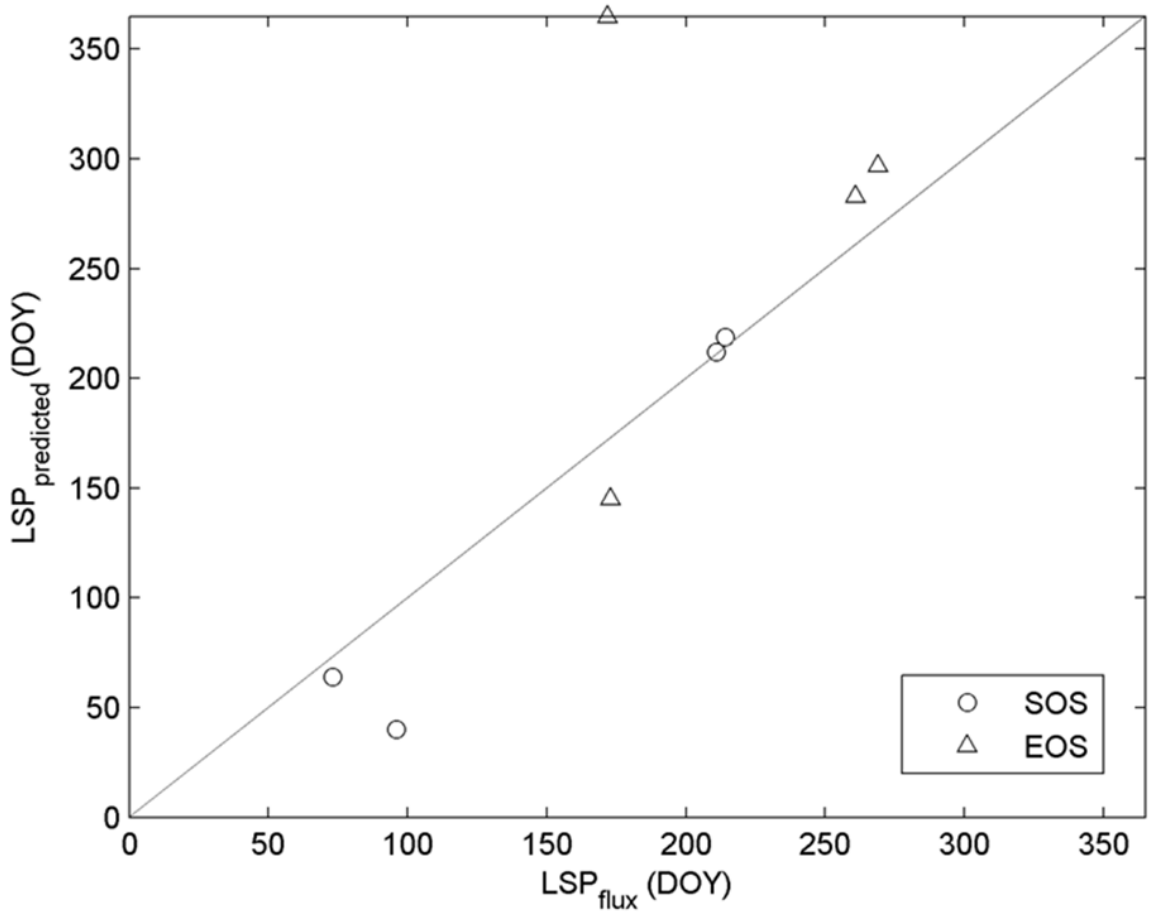

Figure 4: Comparison of LSP estimates derived from flux tower GPP (LSP_{flux}) and from 0.01° resolution MODIS EVI ($LSP_{predicted}$).

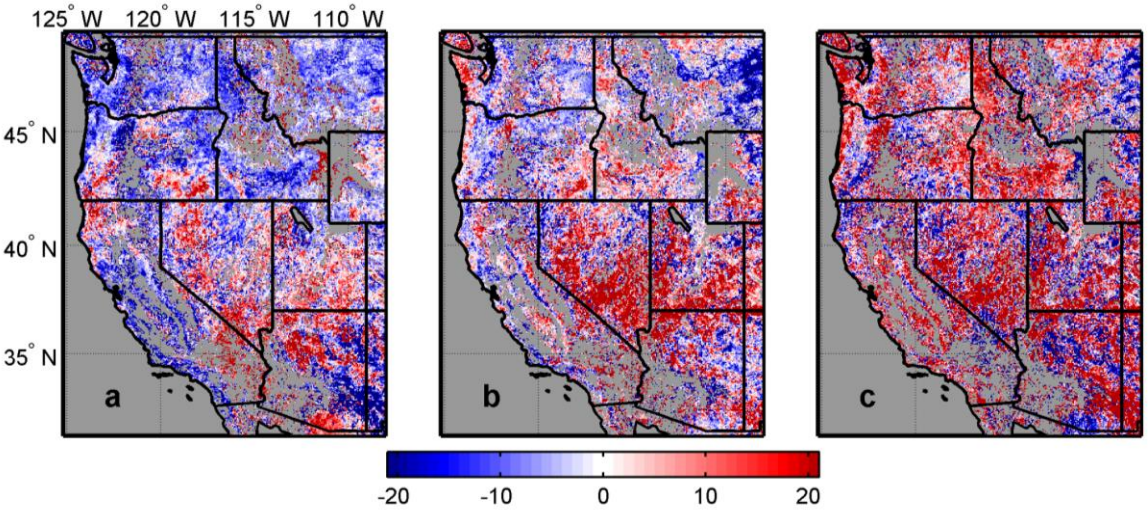

Figure 5: Difference between El Niño and La Niña SOS, EOS, and LOS (a-c, respectively). Negative numbers (blue) indicate earlier (or shorter) events for El Niño relative to La Niña; positive numbers (red) indicate later (or longer) event for El Niño relative to La Niña.

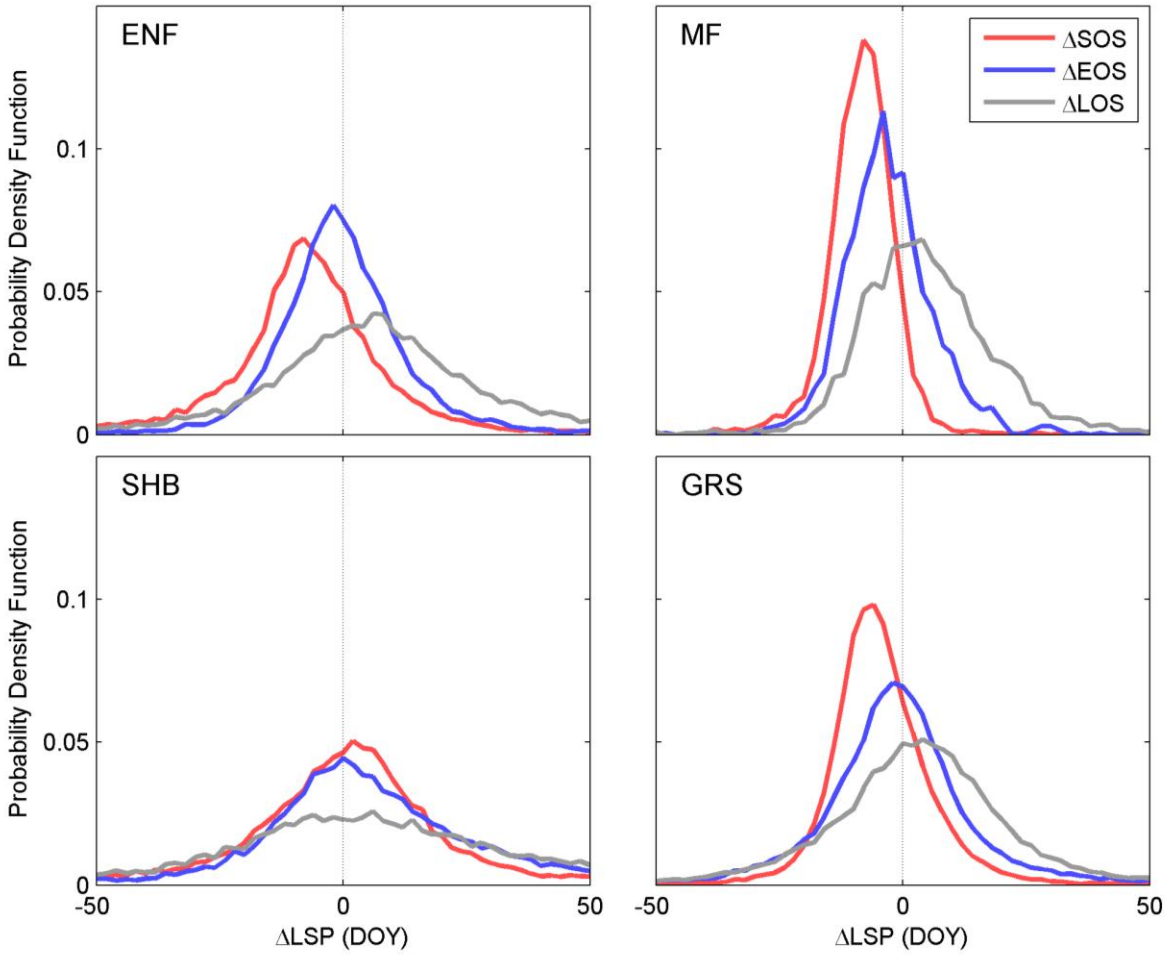

Figure 6: Probability density functions of per-pixel ΔSOS, ΔEOS, and ΔLOS for each PFT. Values less than (greater than) zero indicate advanced (delayed) SOS or EOS and longer (shorter) LOS during El Niño years relative to La Niña years.

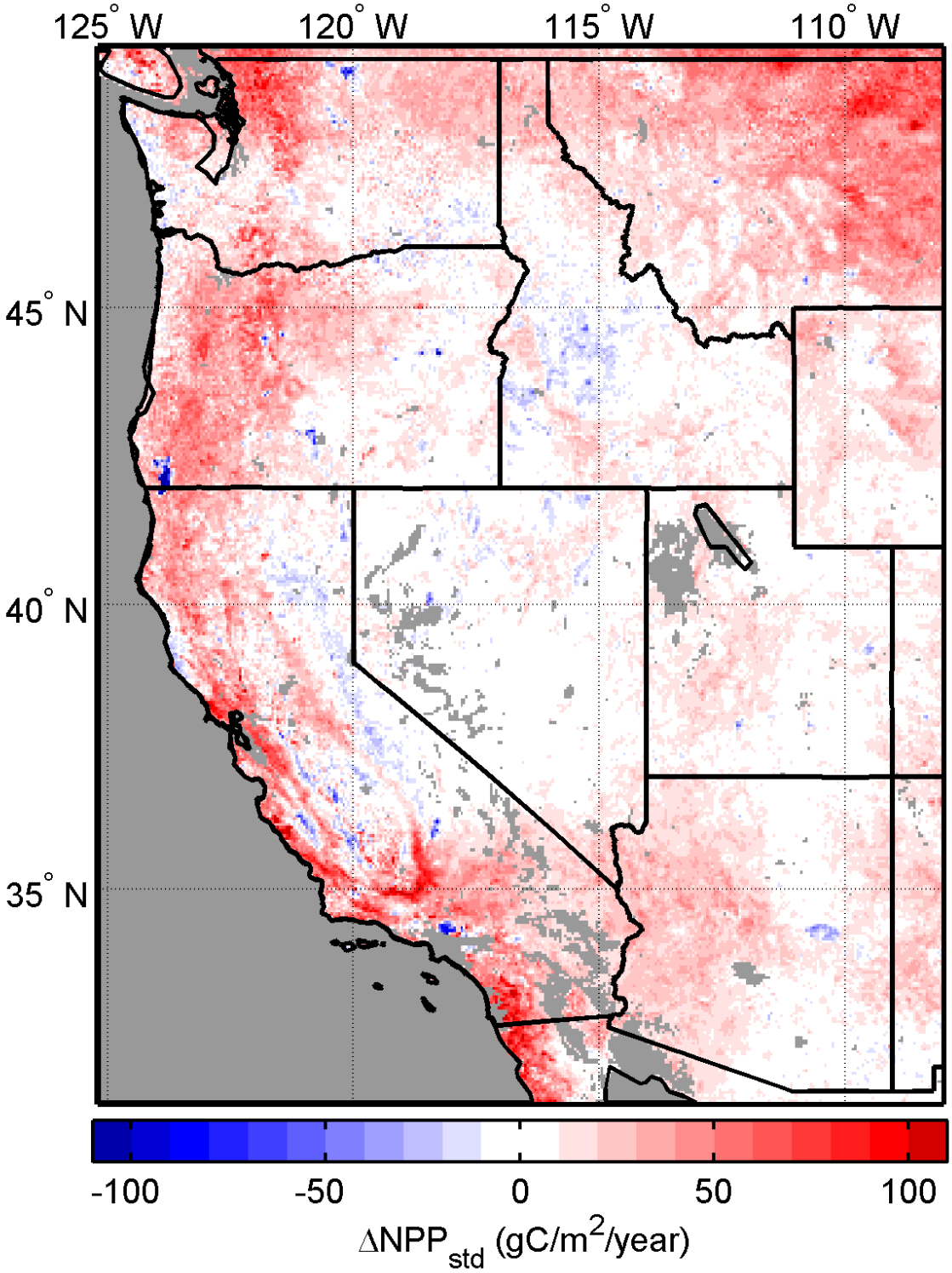

Figure 7: Difference between NPP during El Niño and La Niña years. Positive values (red) indicate greater NPP during El Niño years relative to La Niña years; negative values (blue) indicate reduction in NPP during El Niño years relative to La Niña years.

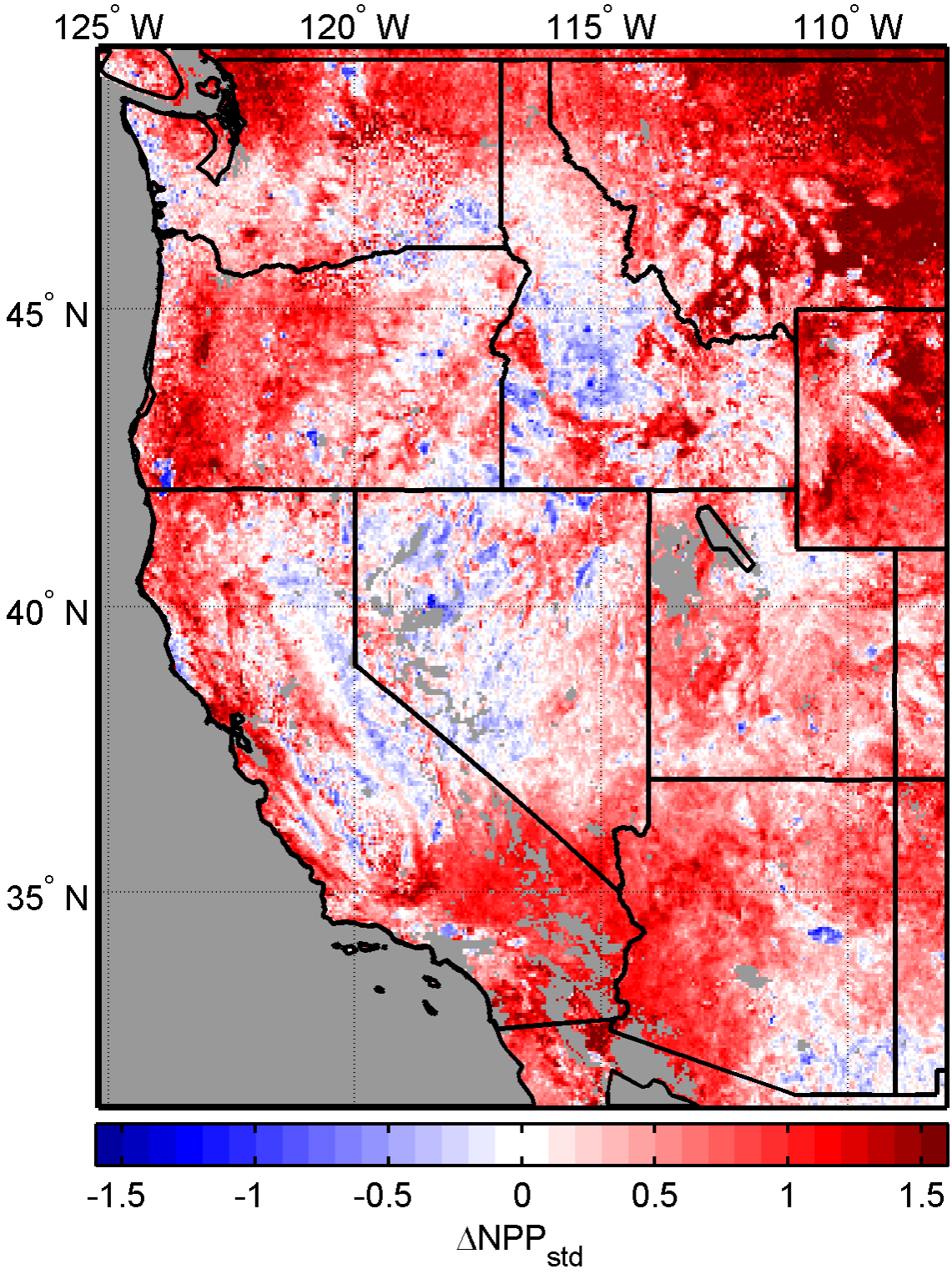

Figure 8: Difference between standardized NPP anomalies (relative to 2000-2010 NPP) during El Niño and La Niña years. Positive values (red) indicate greater NPP during El Niño years relative to La Niña years; negative values (blue) indicate reduction in NPP during El Niño years relative to La Niña years.

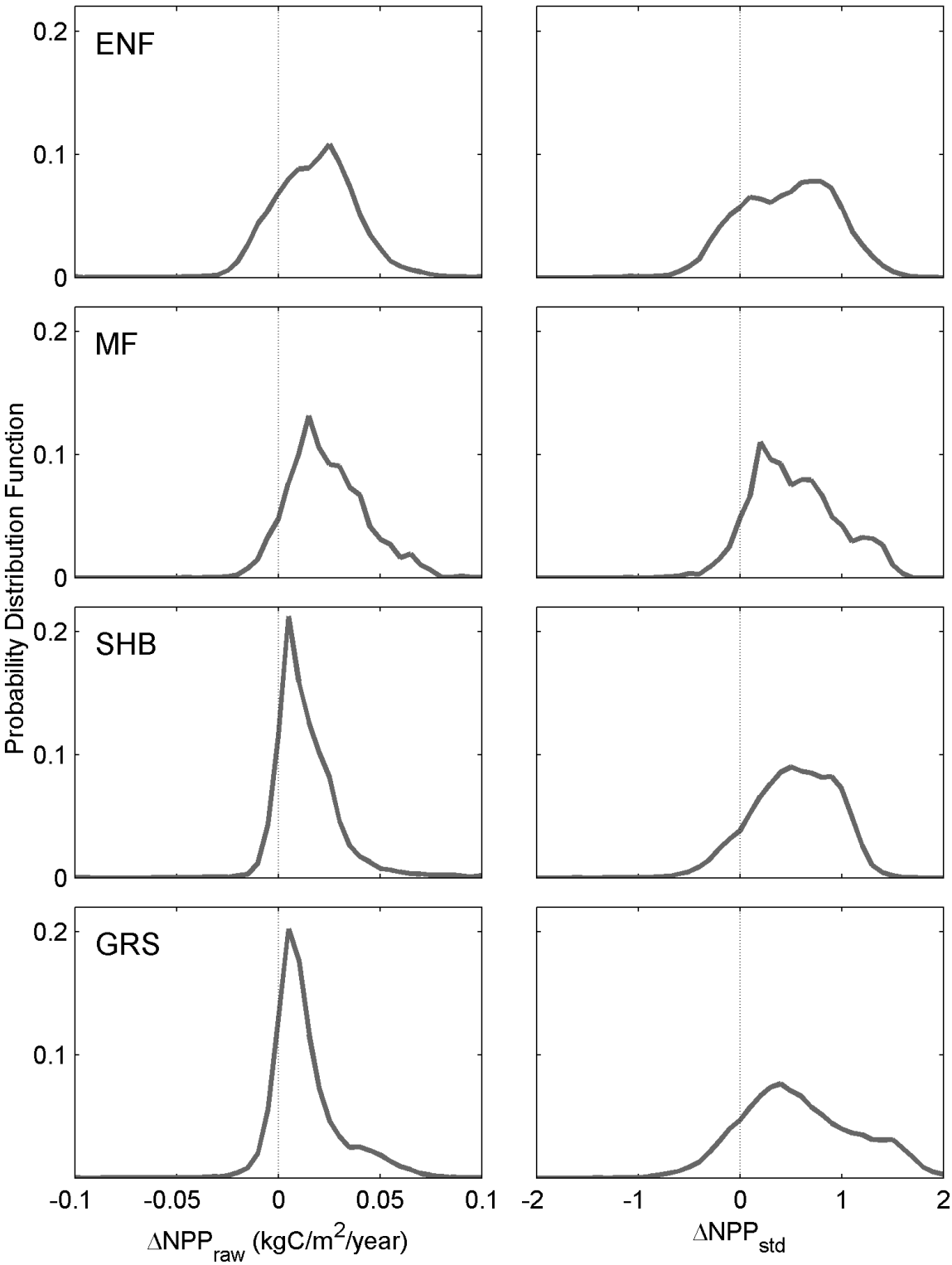

Figure 9: Probability density functions of the difference between per-pixel average NPP (left) and standardized NPP anomalies (right) during El Niño and La Niña years for each PFT.

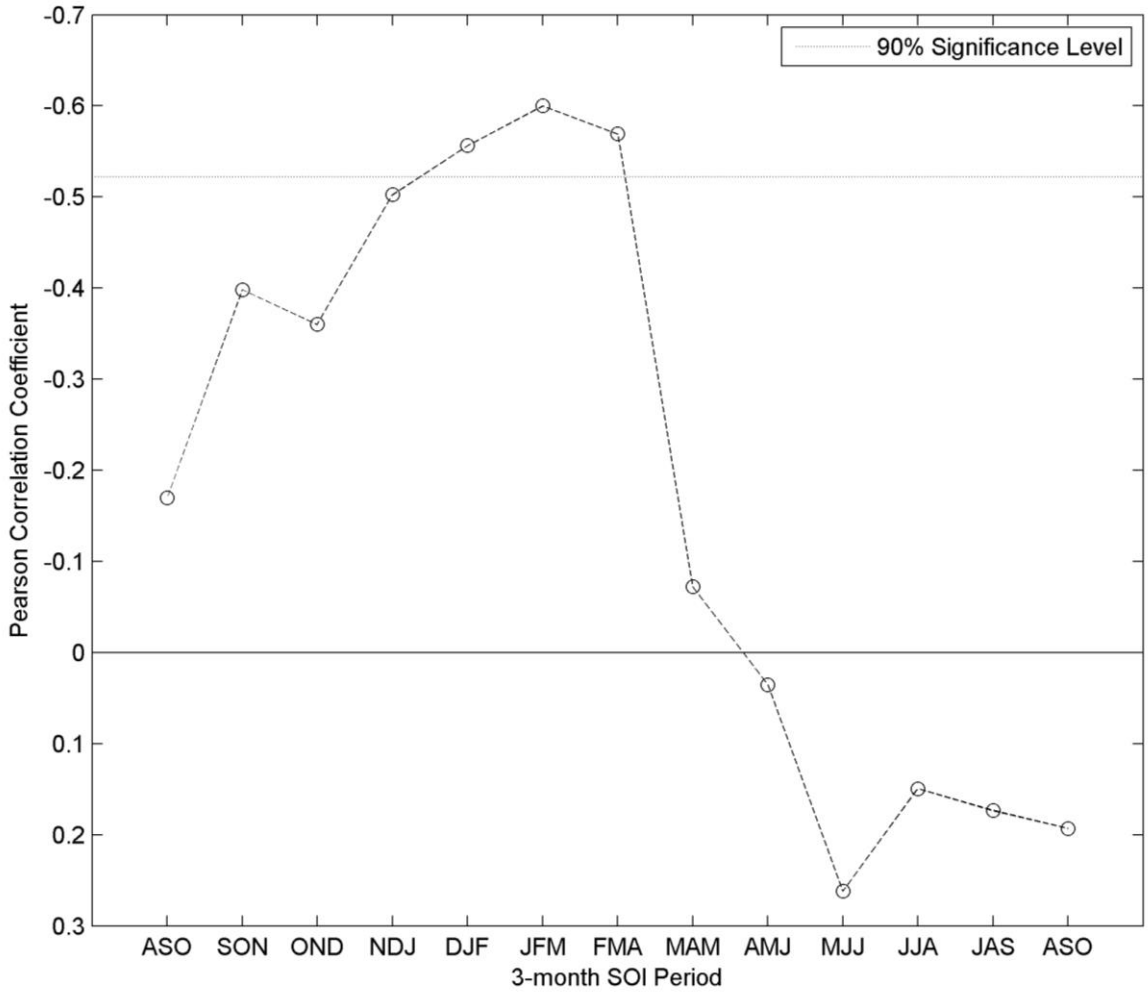

Figure 10: Pearson correlation coefficients between annual total study area NPP and lagged 3-month mean SOI. Note that the y-axis is inverted for display purposes.

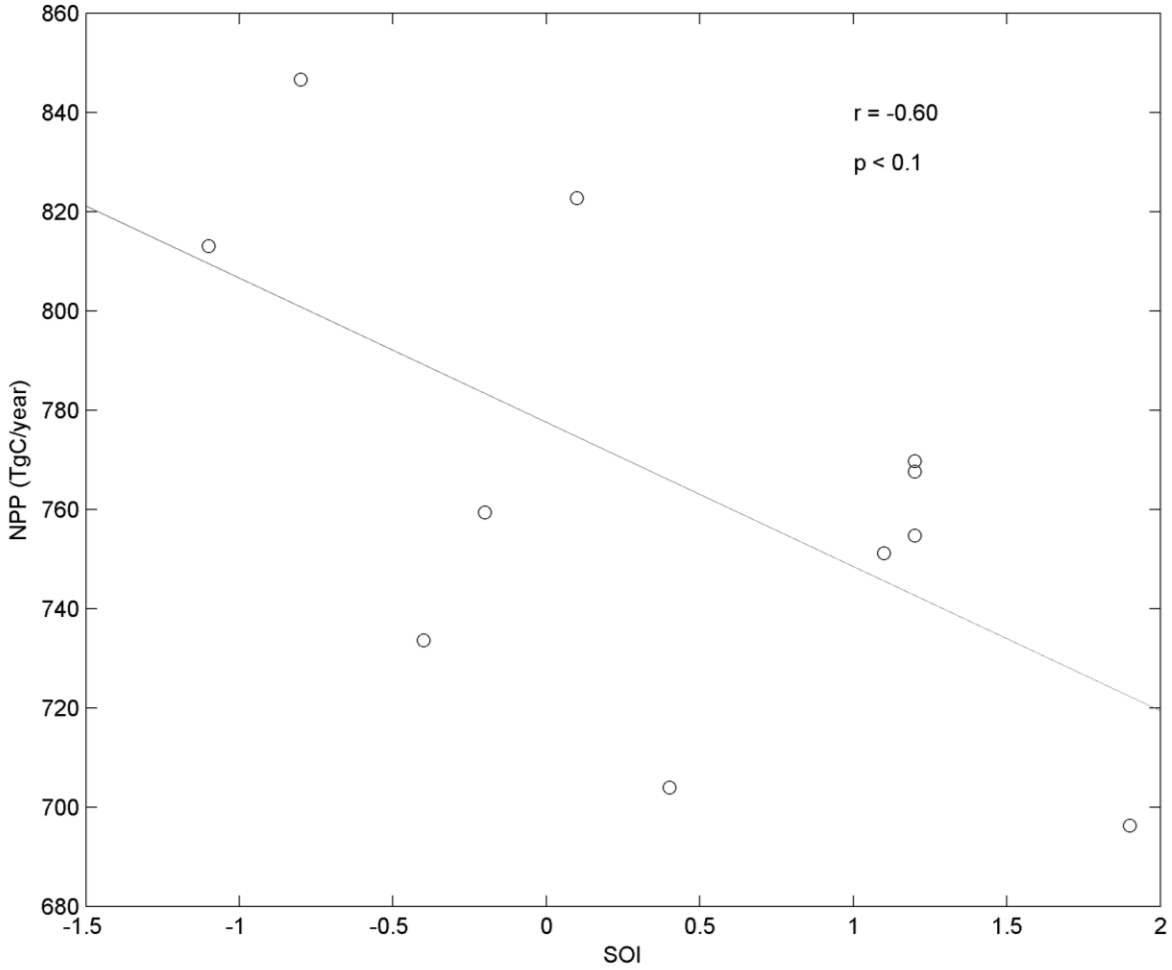

Figure 11: Relationship between annual total study area NPP and JFM-SOI.

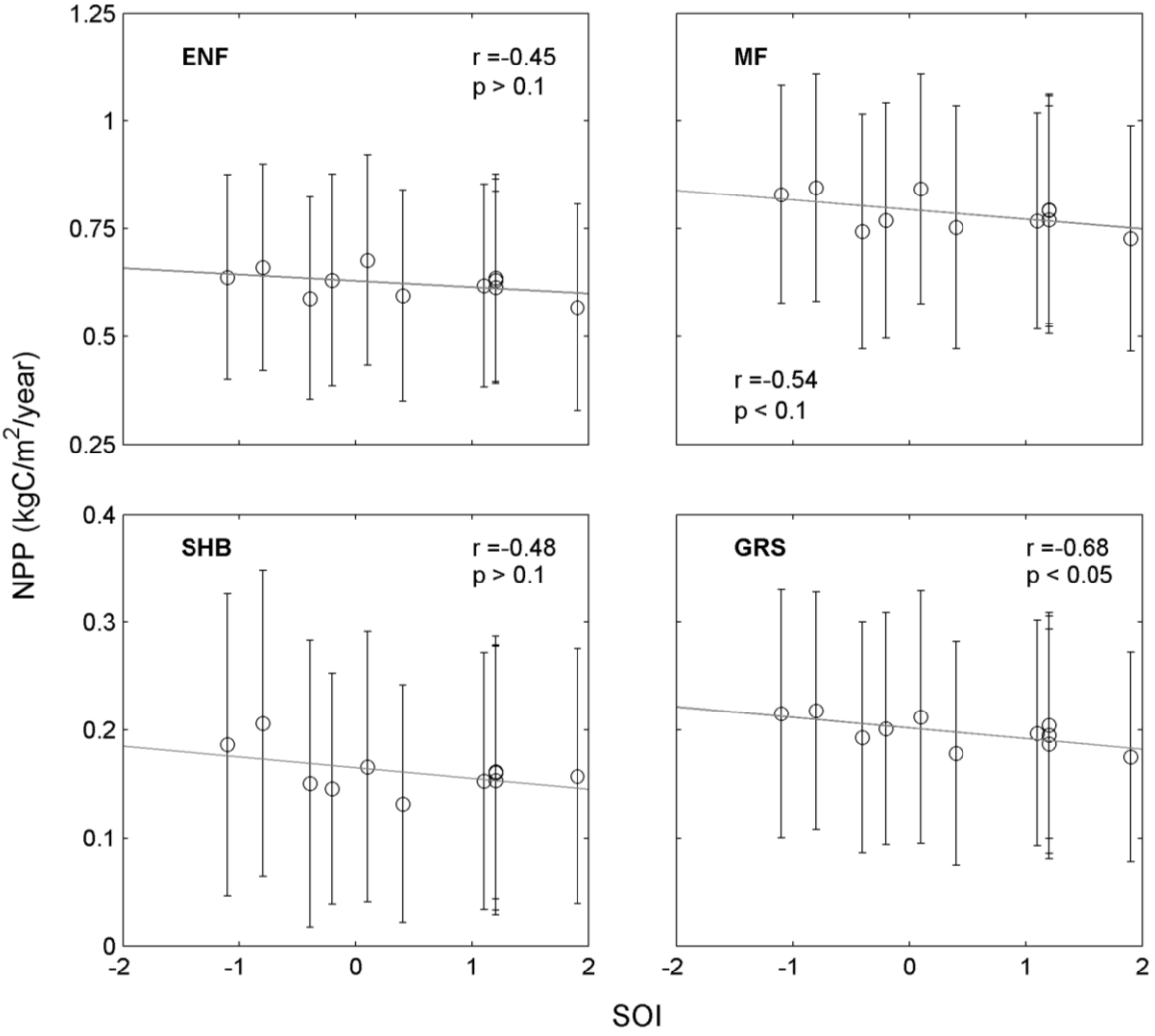

Figure 12: Relationships between annual average NPP and JFM-SOI for each PFT. Error bars represent one standard deviation of NPP for all pixels within a given PFT.

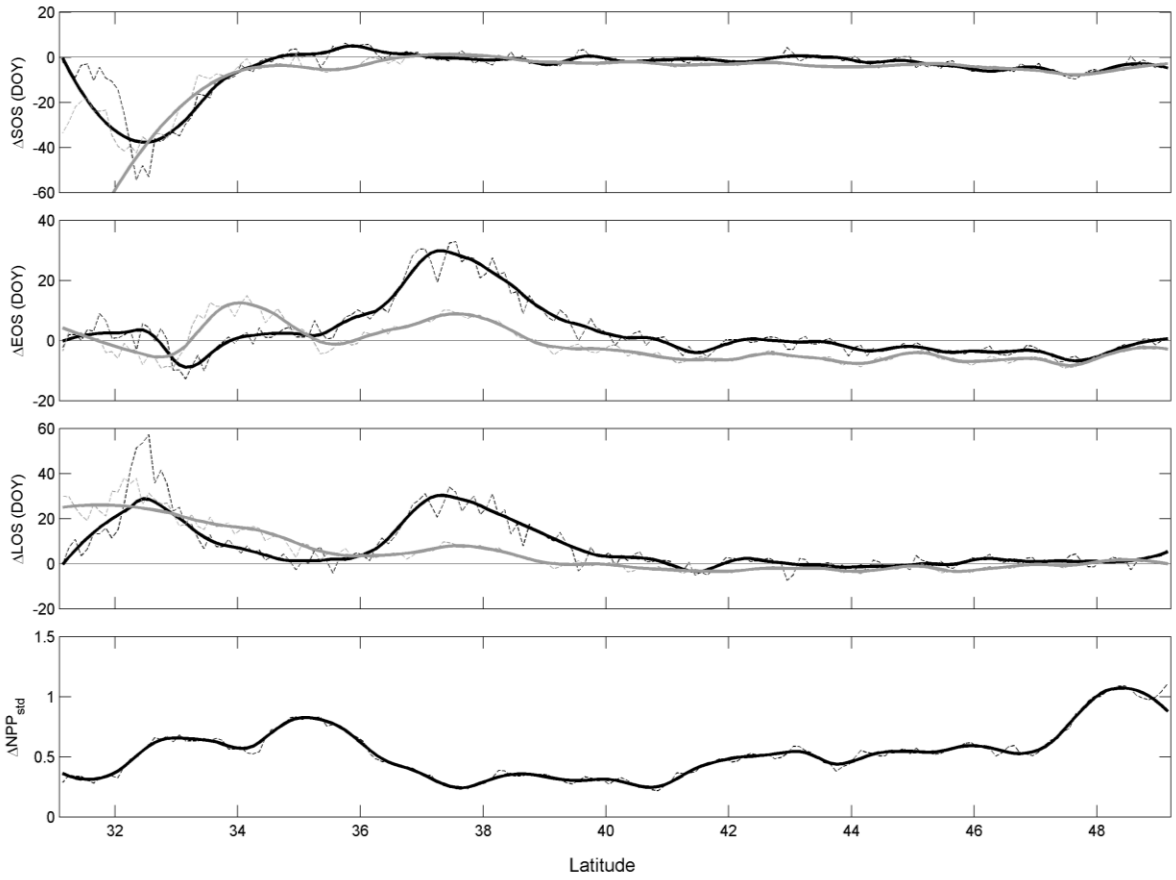

Figure 13: Average zonal differences between SOS, EOS, LOS, and standardized NPP anomalies during El Niño and La Niña events. For ΔSOS, ΔEOS, and ΔLOS, positive values indicate later (or longer) LSP during El Niño years relative to La Niña years. Black lines indicate LSP derived in this study, gray lines indicate LSP derived from MLCD. For ΔNPP_{std}, positive values indicate increased NPP during El Niño years relative to La Niña years. Dashed lines represent raw data, while dark lines are smoothed using robust loess.

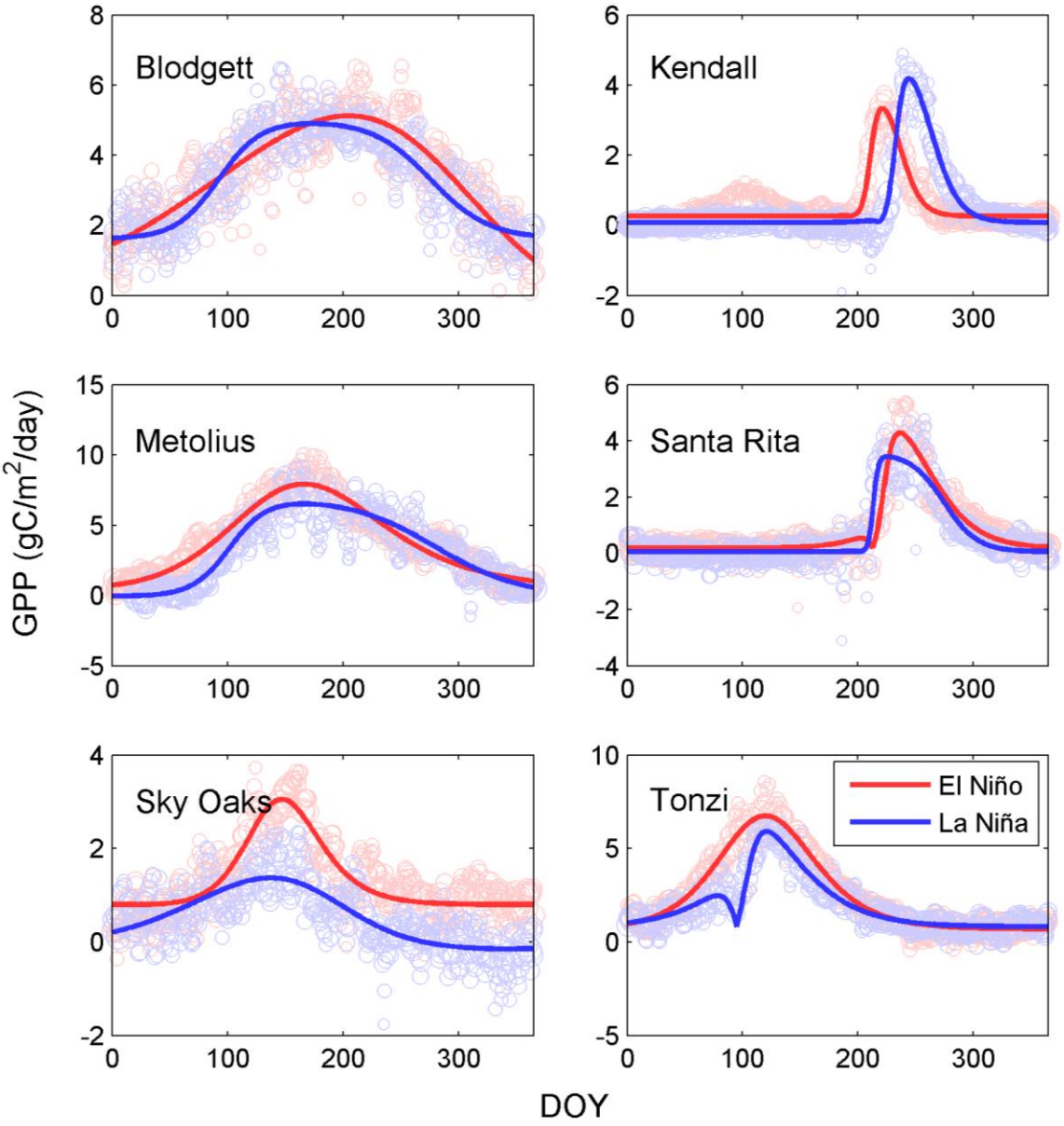

Figure 14: Seasonal trajectories of daily flux tower GPP during El Niño (red) and La Niña (blue) years at each flux site.

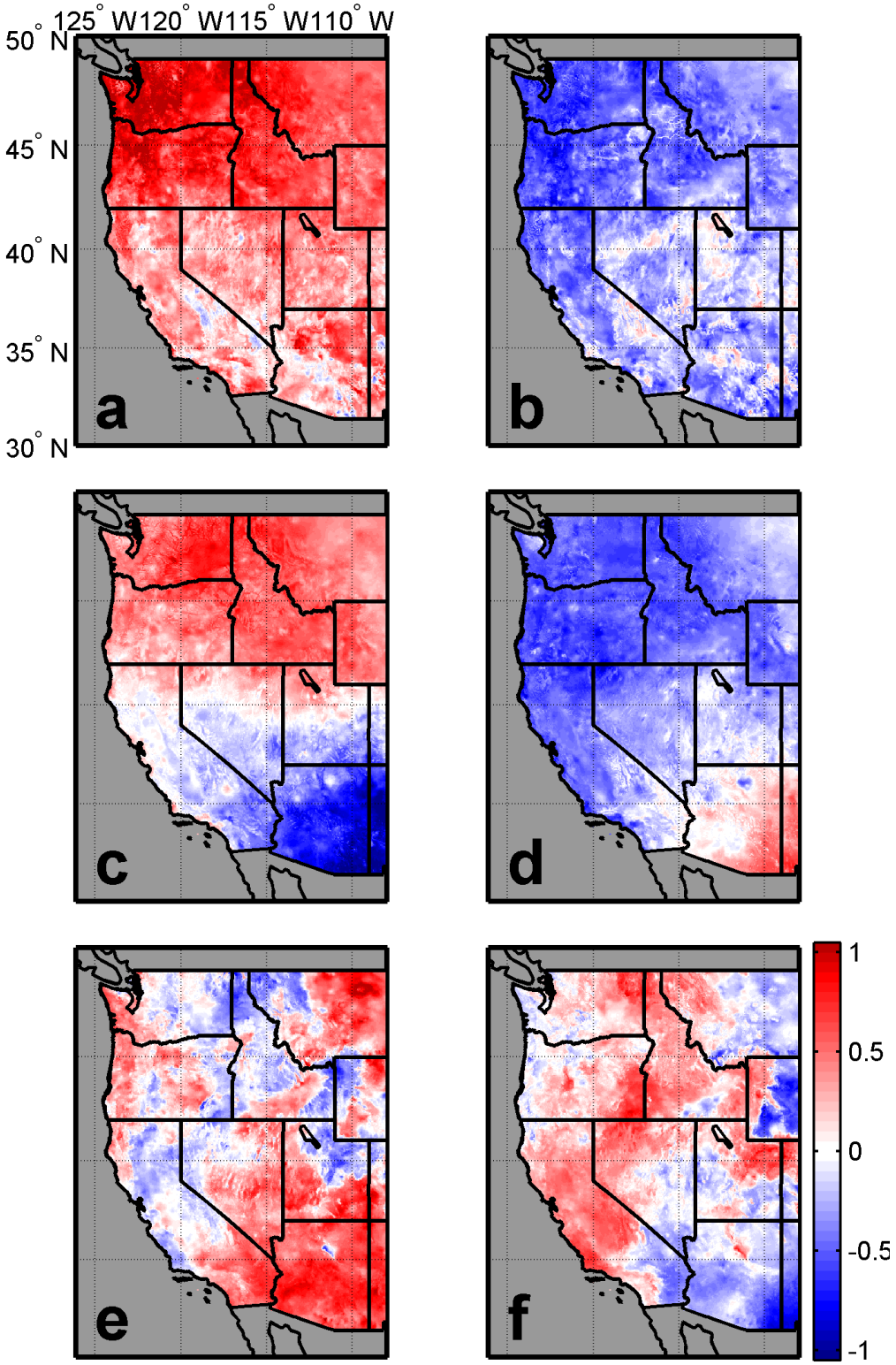

Figure 15: February through April z-scores of average daily minimum temperature (a & b), average daily maximum temperature (c & d), and precipitation (e & f) during El Niño (left column) and La Niña (right column) years, relative to mean 2000-2011 climatology.

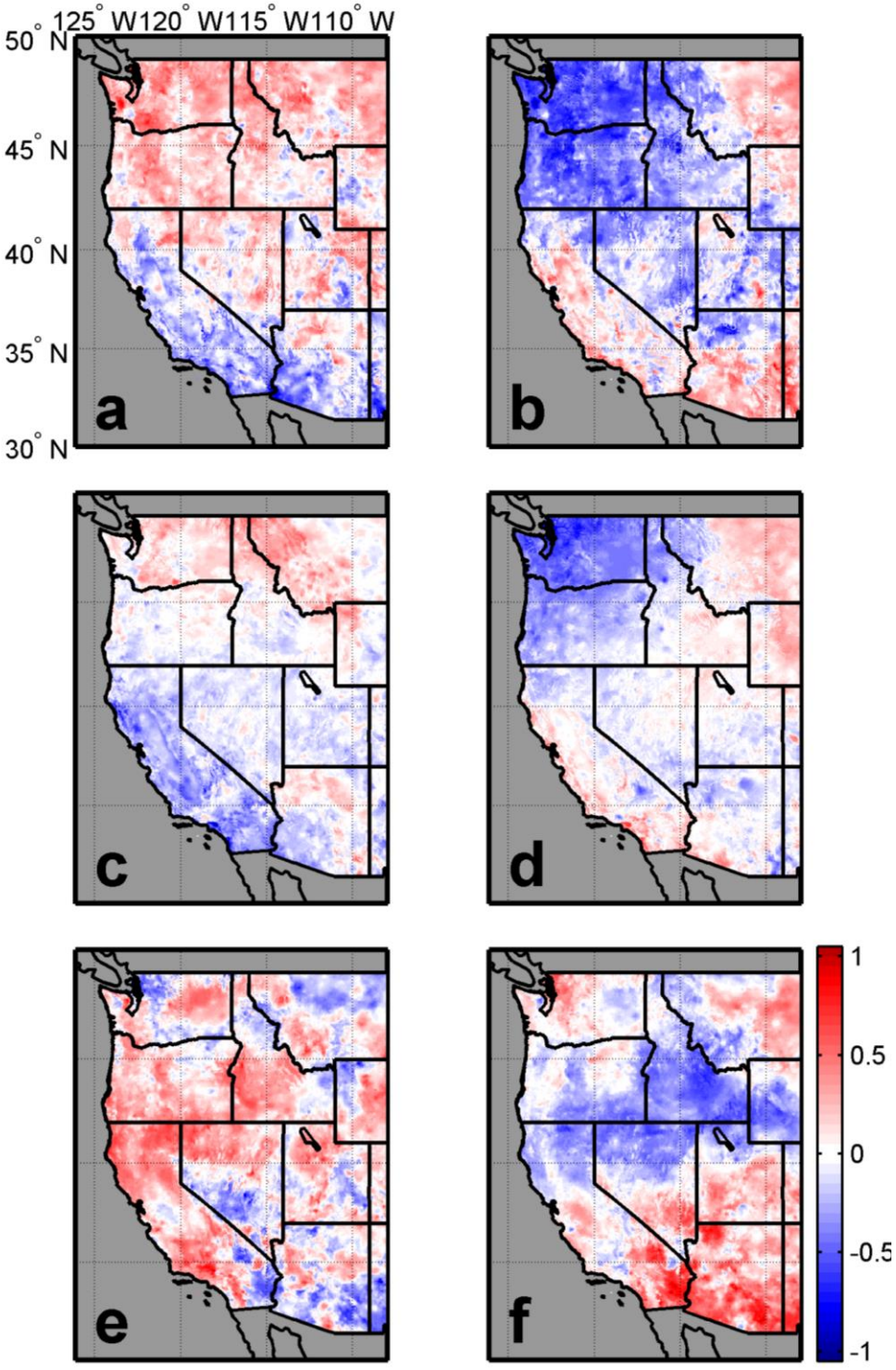

Figure 16: May through July z-scores of average daily minimum temperature (a & b), average daily maximum temperature (c & d), and precipitation (e & f) during El Niño (left column) and La Niña (right column) years, relative to mean 2000-2011 climatology.

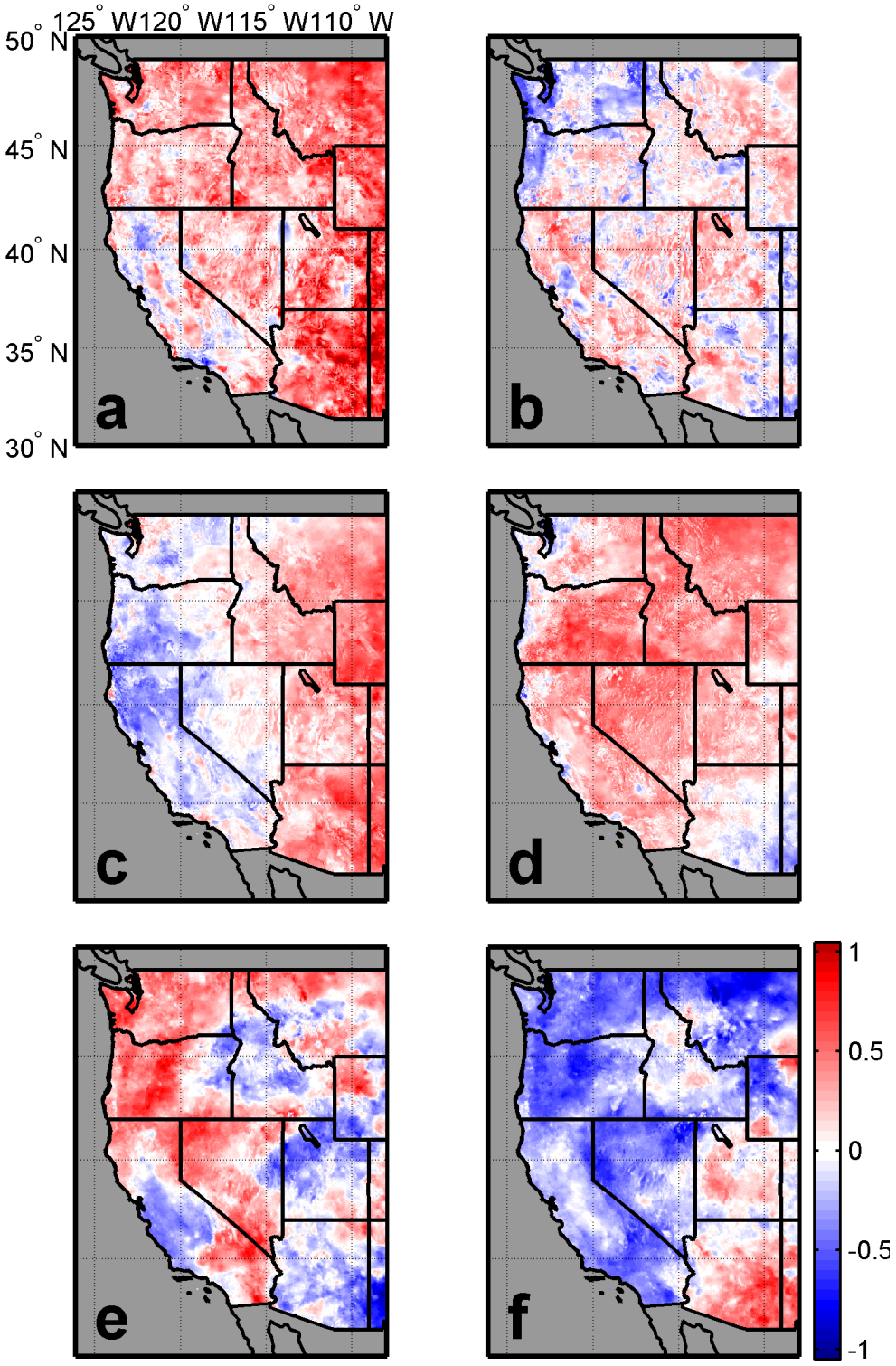

Figure 17: August through October z-scores of average daily minimum temperature (a & b), average daily maximum temperature (c & d), and precipitation (e & f) during El Niño (left column) and La Niña (right column) years, relative to mean 2000-2011 climatology.

APPENDIX

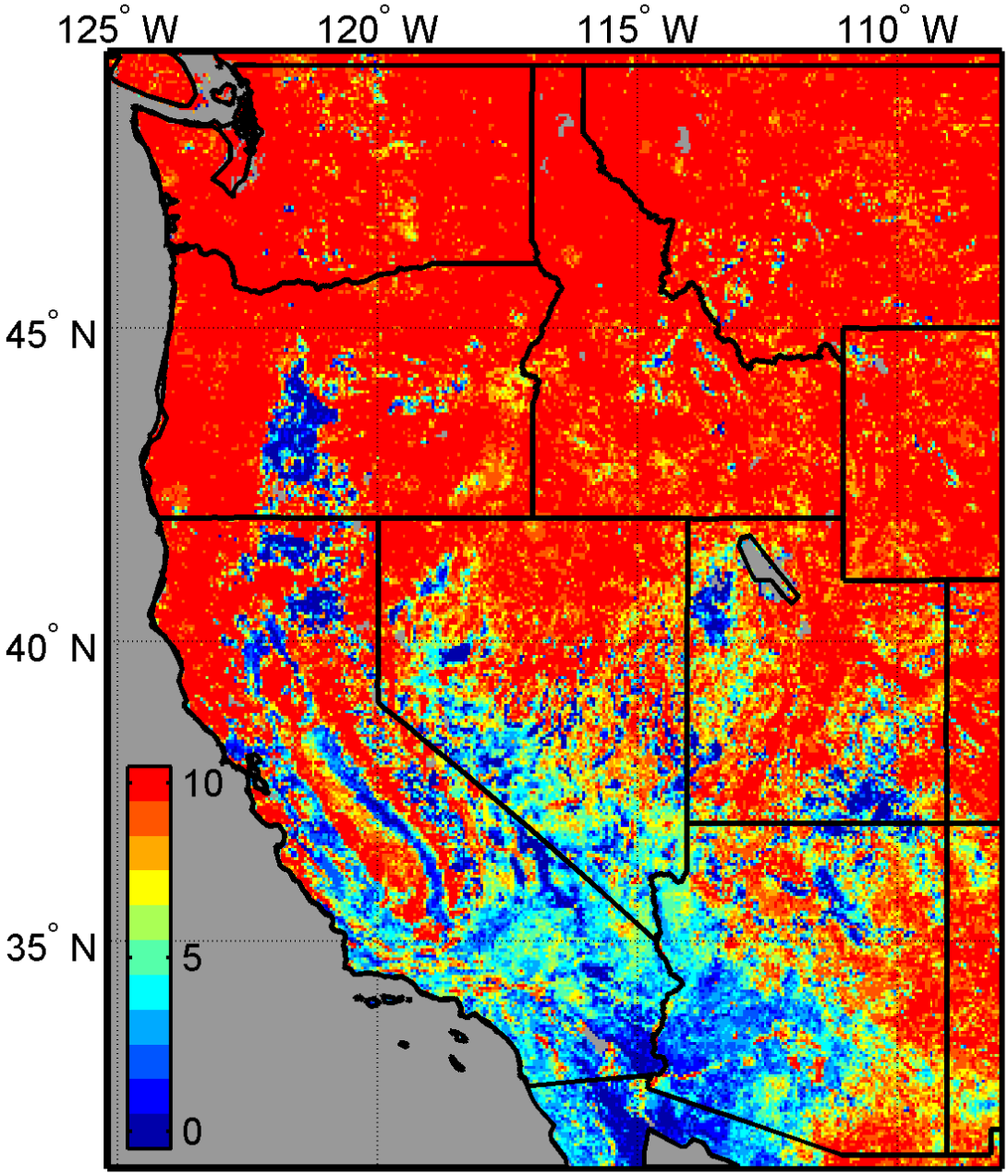

Figure A1: Number of annual MLCD LSP estimates from 2001-2010.

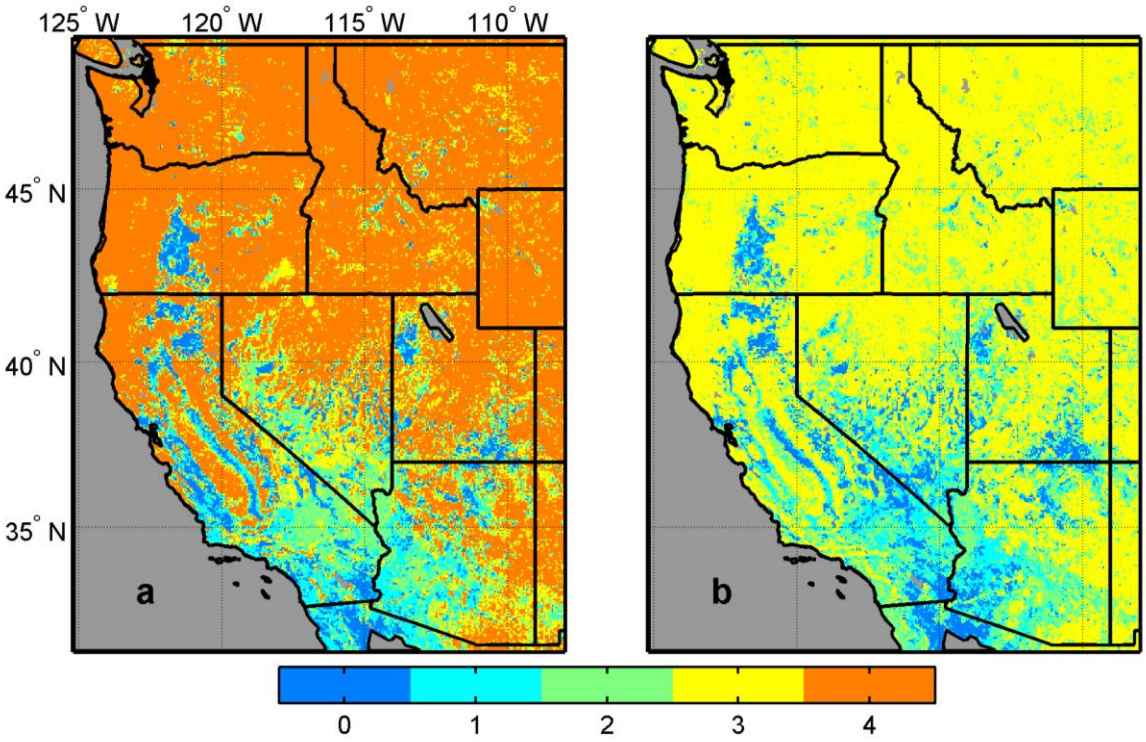

Figure A2: Number of annual MLCD LSP estimates in El Niño (a) and La Niña (b) years.

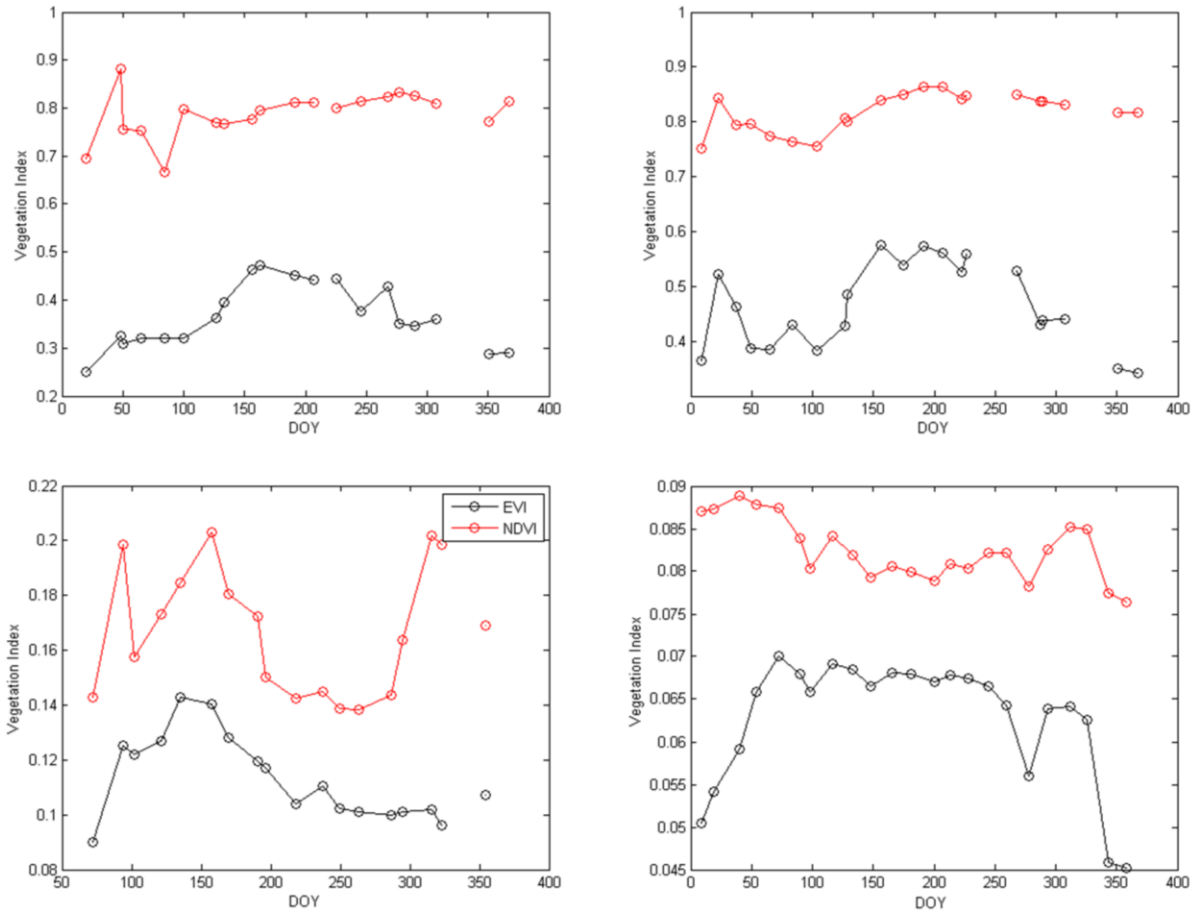

Figure A3: Seasonal MOD13A2 NDVI (red) and EVI (black) observations from select pixels within the study area.

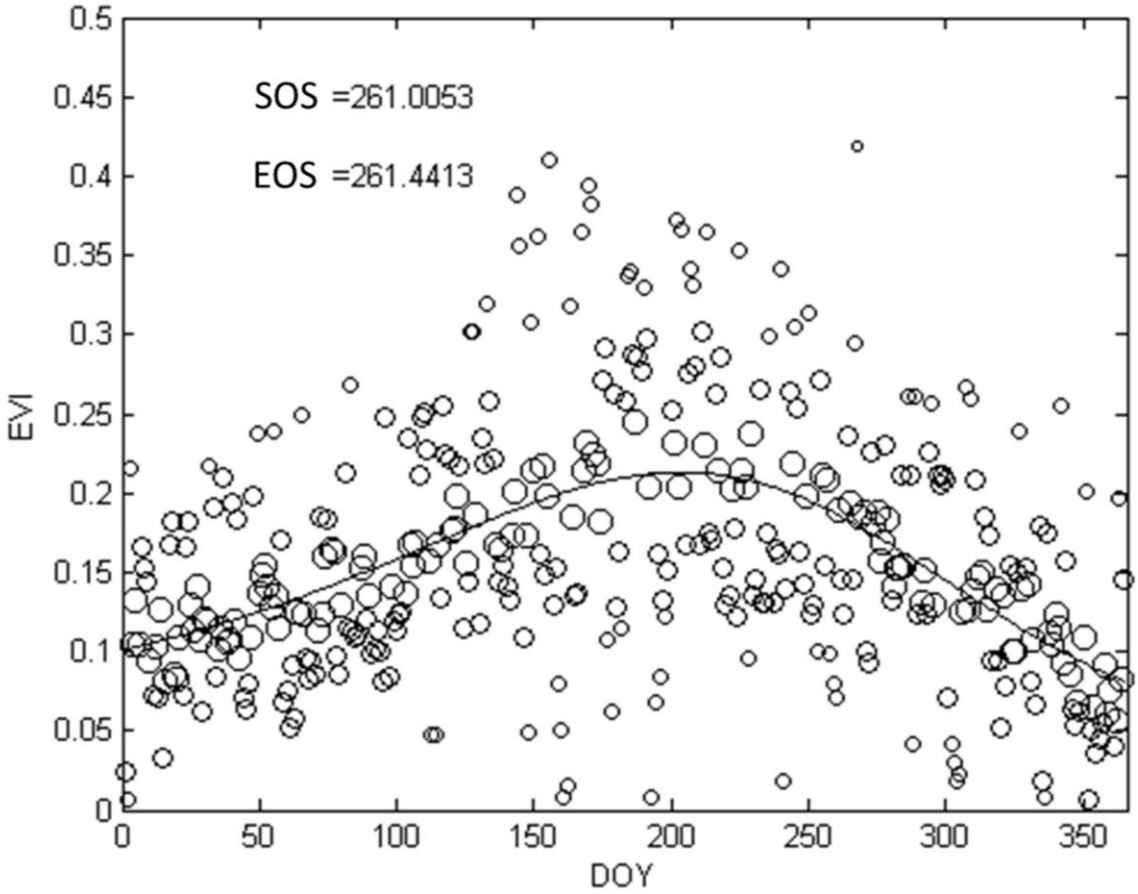

Figure A4: Example of a fitted difference logistic curve (with LSP metrics derived from inflection points) where the green-up and senescence logistic functions simultaneously influence the curve.

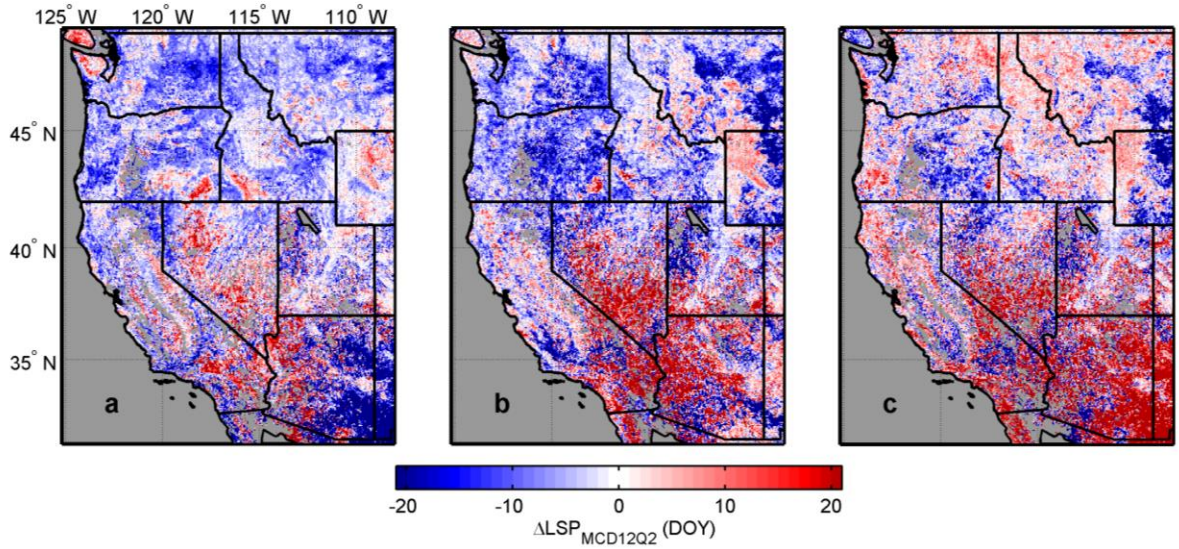

Figure A5: Difference between El Niño and La Niña SOS, EOS, and LOS (a-c, respectively) derived from MLCD. Negative numbers (blue) indicate earlier (or shorter) LSP events for El Niño years relative to La Niña years; positive numbers (red) indicate later (or longer) LSP events for El Niño relative to La Niña.

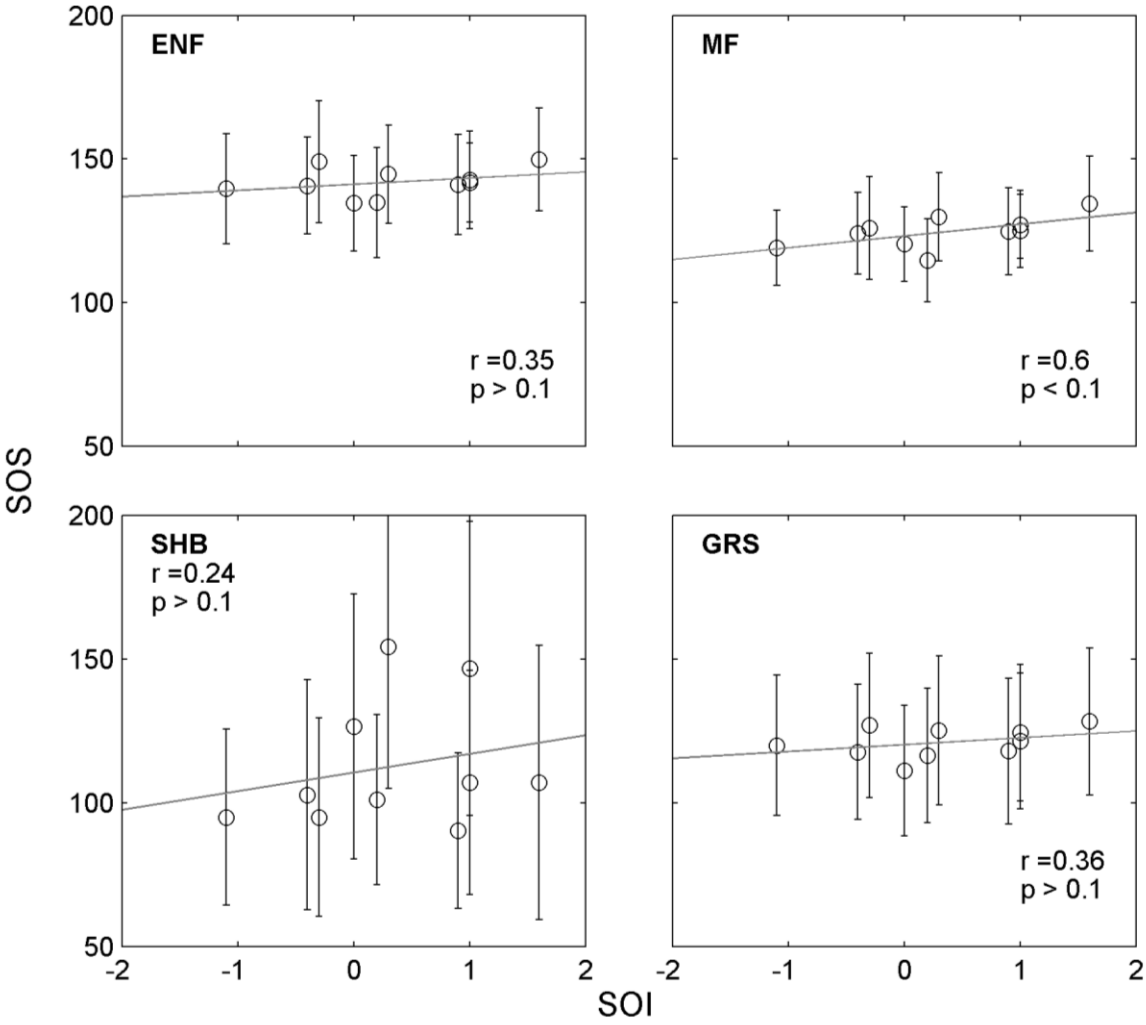

Figure A6: Relationships between annual average SOS and FMA-SOI for each PFT. Error bars represent one standard deviation of SOS for all pixels within a given PFT.

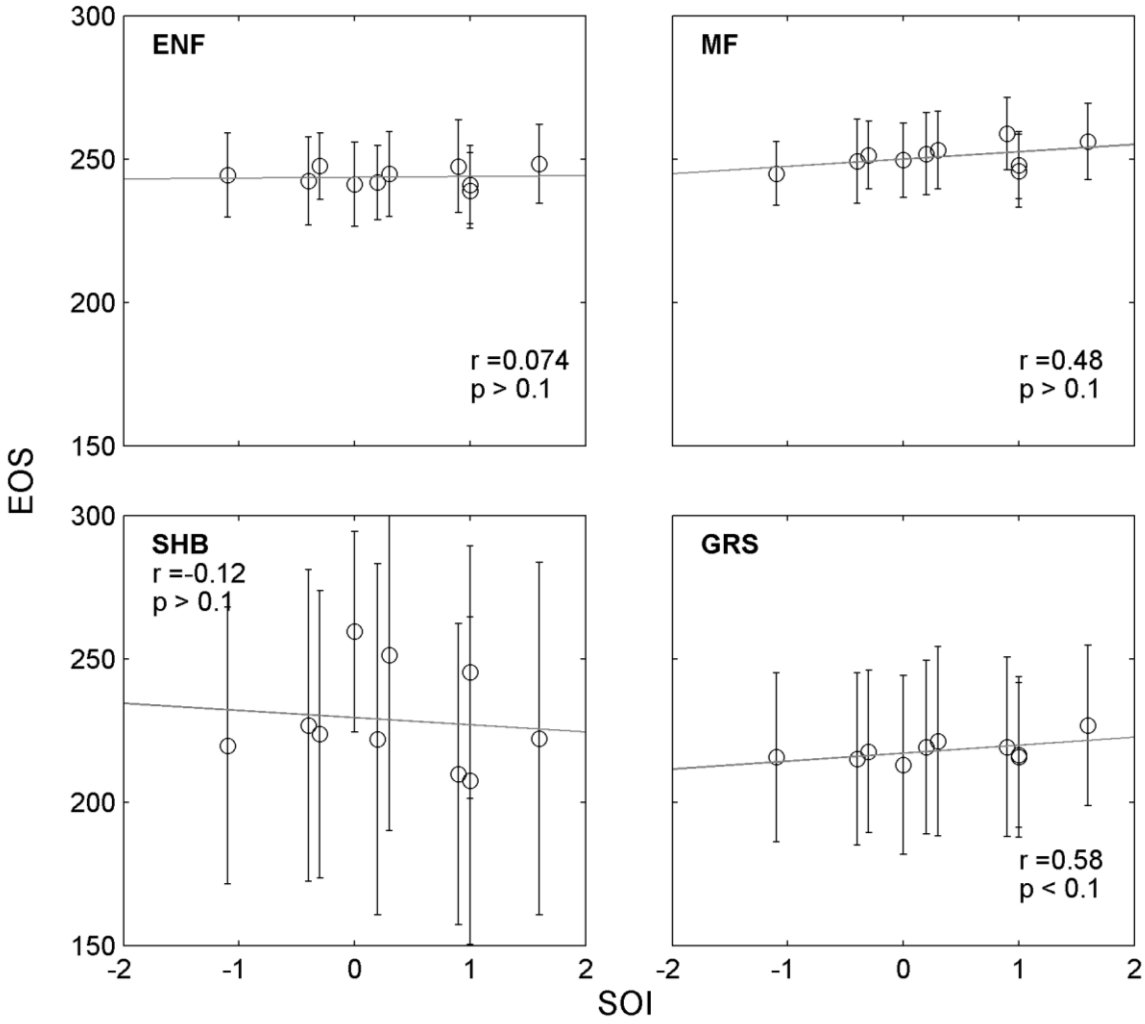

Figure A7: Relationships between annual average EOS and FMA-SOI for each PFT. Error bars represent one standard deviation of EOS for all pixels within a given PFT.

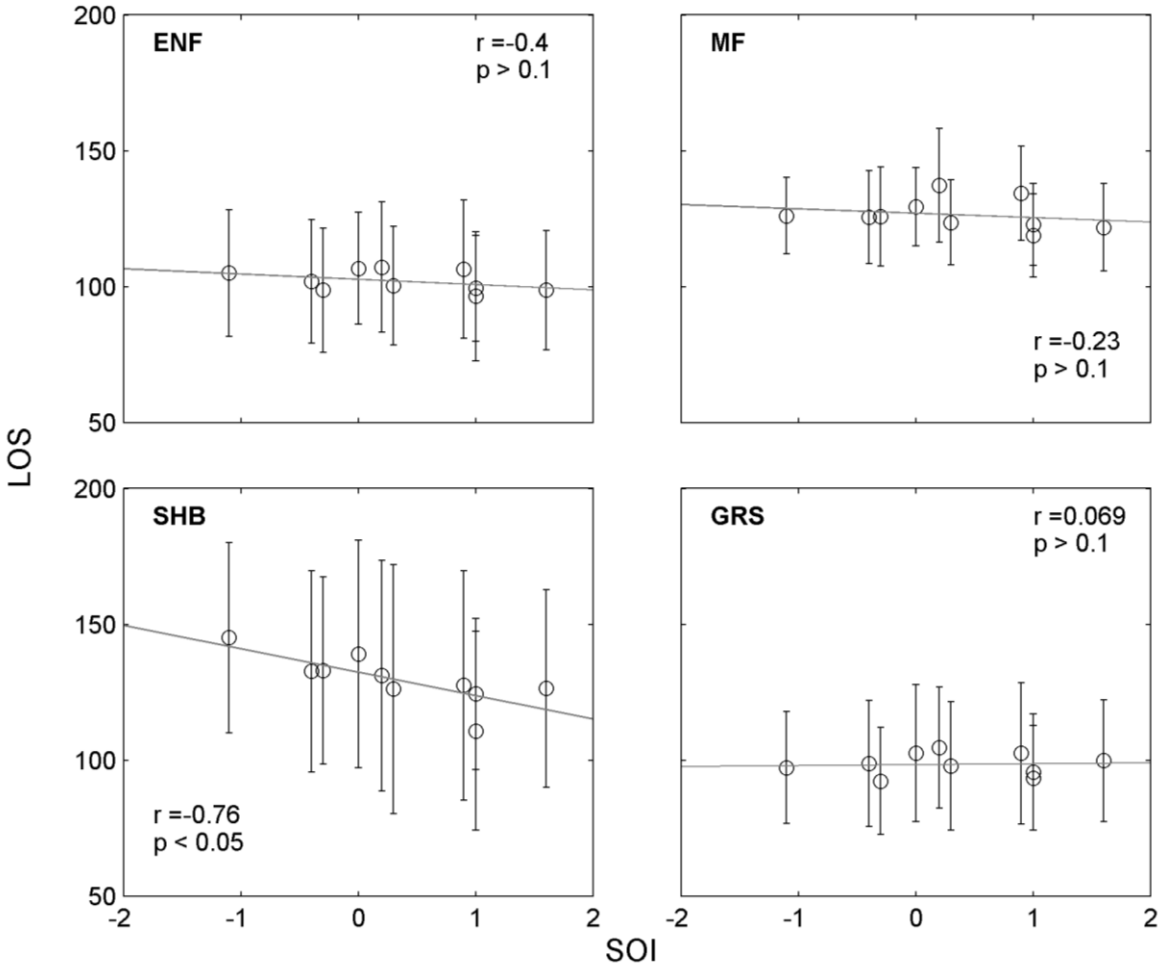

Figure A8: Relationships between annual average LOS and FMA-SOI for each PFT. Error bars represent one standard deviation of LOS for all pixels within a given PFT.

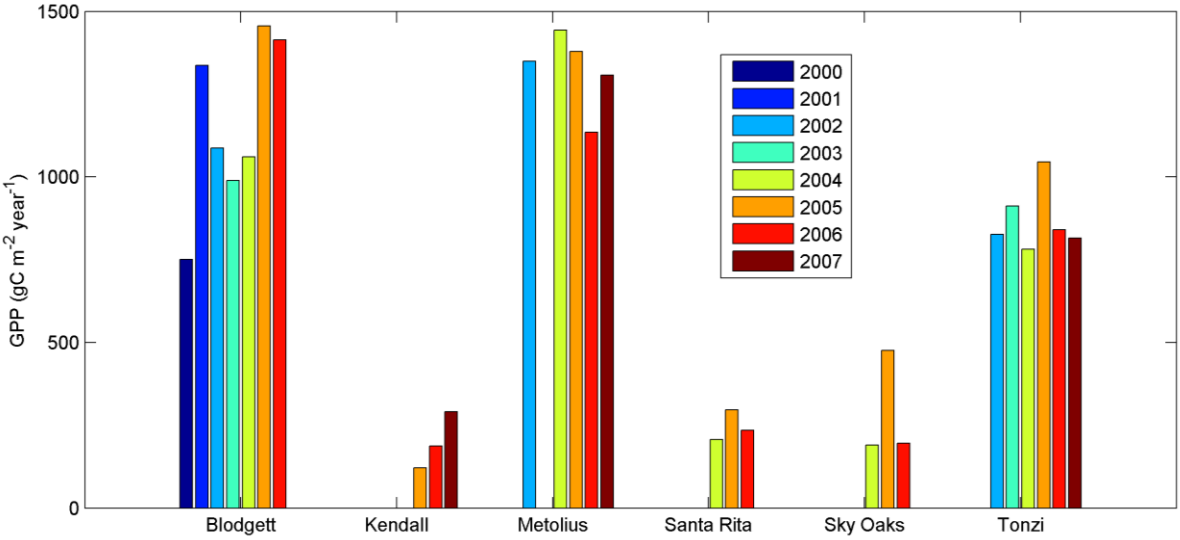

Figure A9: Annual GPP at the six eddy covariance flux towers used in this study. Only years with fewer than 40 missing daily GPP values were used in calculation of annual GPP. Only days with valid GPP observations across all years were used in calculation of annual GPP at a given site. At Blodgett, for example, GPP values were missing from DOY 339-365 for year 2004, so only DOY 1-338 were used for calculation of annual GPP in all years at the Blodgett flux site.

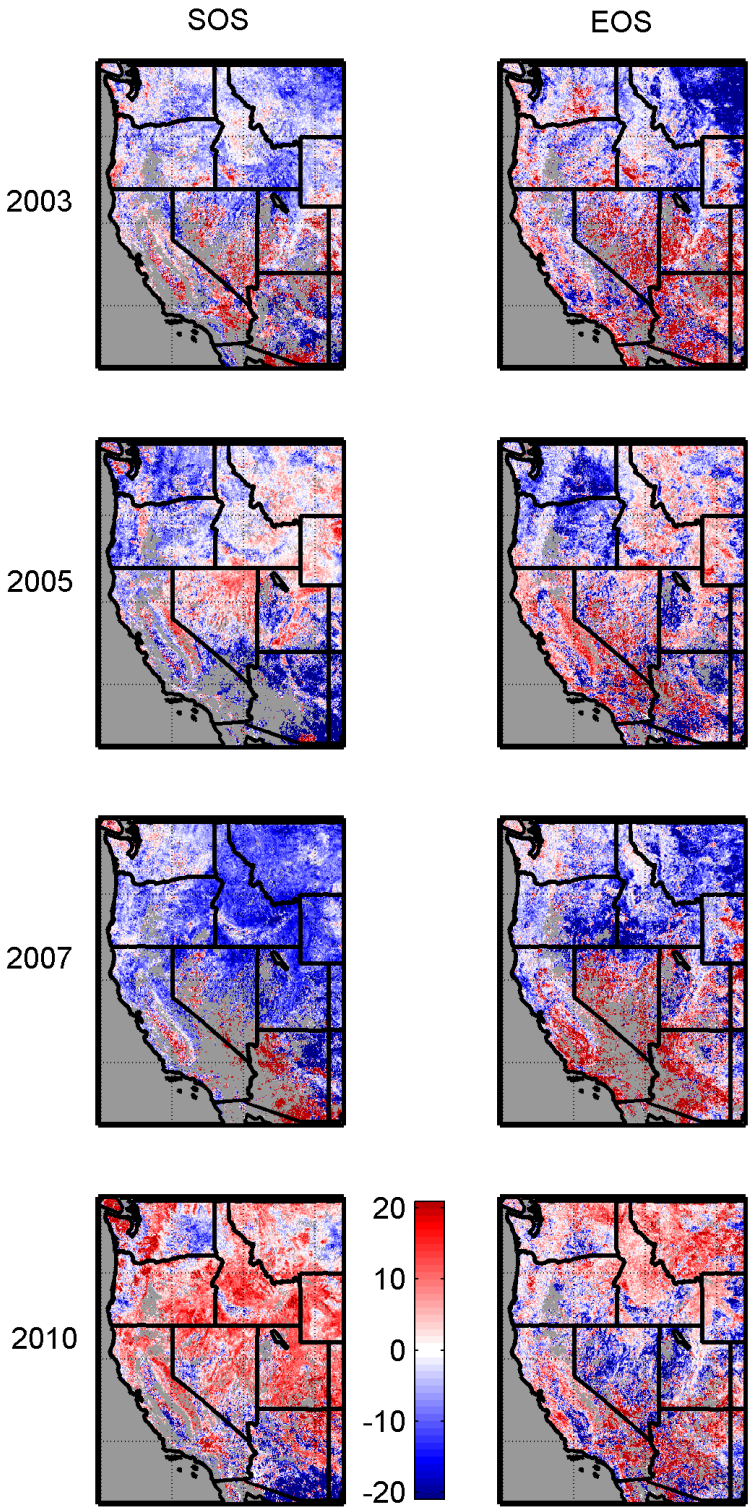

Figure A10: Difference between annual SOS (left column) and EOS (right column) during El Niño years and per-pixel mean (2001-2010) SOS and EOS. Negative values (blue) indicate earlier SOS or EOS relative to 2001-2010 mean, while positive values (red) indicate later SOS or EOS relative to 2001-2010 mean.

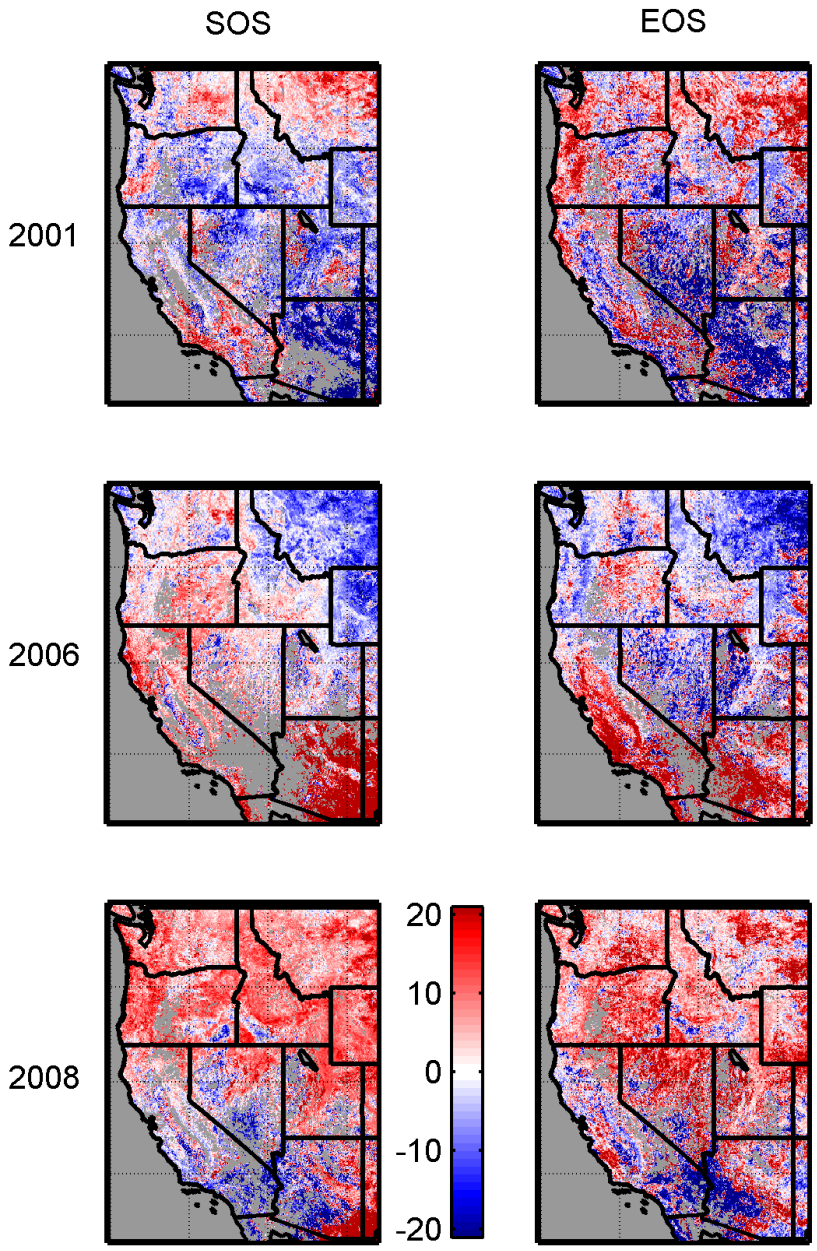

Figure A11: Difference between annual SOS (left column) and EOS (right column) during La Niña years and per-pixel mean (2001-2010) SOS and EOS. Negative values (blue) indicate earlier SOS or EOS relative to 2001-2010 mean, while positive values (red) indicate later SOS or EOS relative to 2001-2010 mean.

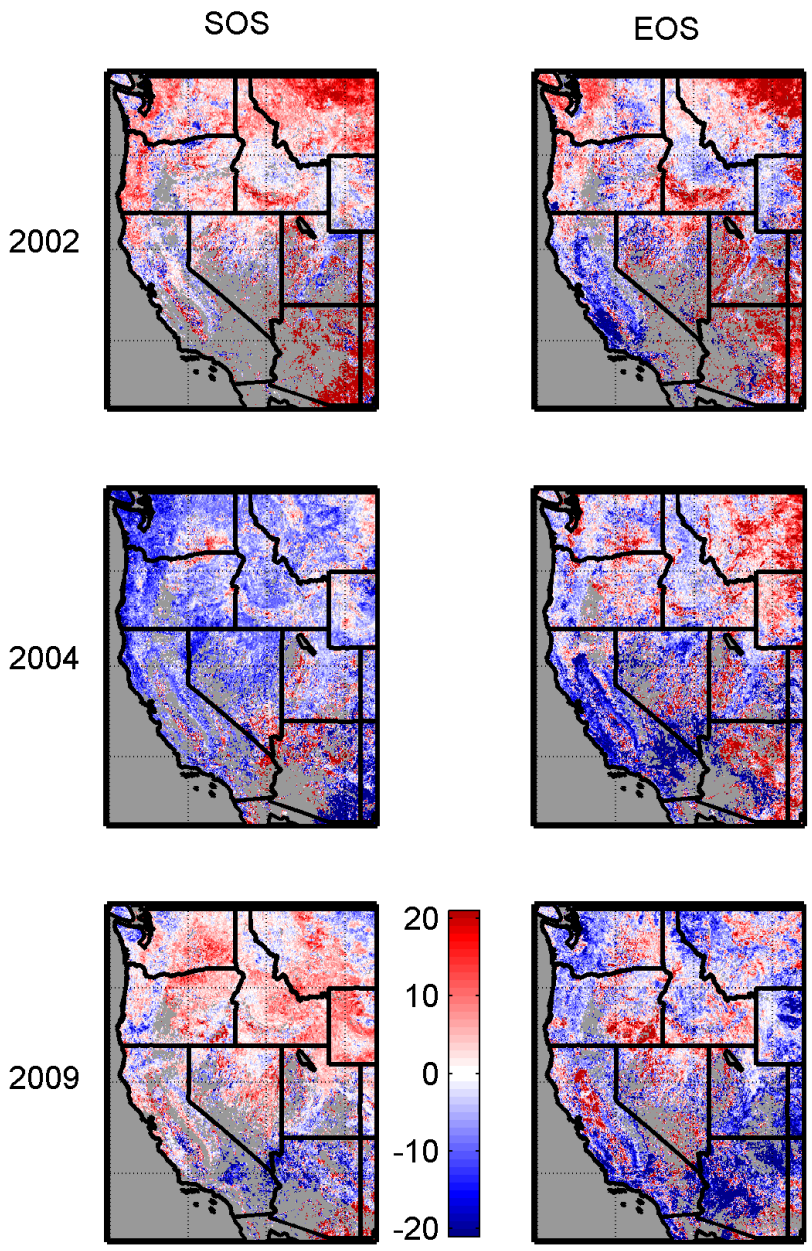

Figure A12: Difference between annual SOS (left column) and EOS (right column) during neutral years and per-pixel mean (2001-2010) SOS and EOS. Negative values (blue) indicate earlier SOS or EOS relative to 2001-2010 mean, while positive values (red) indicate later SOS or EOS relative to 2001-2010 mean.

REFERENCES

Anyamba, A., C. J. Tucker, and J. R. Eastman (2001), NDVI anomaly patterns over Africa during the 1997/98 ENSO warm event, *International Journal of Remote Sensing*, *22*(10), 1847–1859, doi:10.1080/01431160010029156.

Anyamba, A., C. J. Tucker, and R. Mahoney (2002), From El Nino to La Nina: vegetation response patterns over East and Southern Africa during the 1997-2000 period, *Journal of Climate*, 3096–3103.

Archibold, O. W. (1995), *Ecology of World Vegetation*, Chapman & Hall, London, UK.

Baldocchi, D. et al. (2001), FLUXNET: a new tool to study the temporal and spatial variability of ecosystem-scale carbon dioxide, water vapor, and energy flux densities, *Bulletin of the American Meteorological Society*, *82*(11), 2415–2434.

Baldocchi, D. D. (2003), Assessing the eddy covariance technique for evaluating carbon dioxide exchange rates of ecosystems: past, present and future, *Global Change Biology*, *9*, 479–492.

Bauerle, W. L., R. Oren, D. A. Way, S. S. Qian, P. C. Stoy, P. E. Thornton, J. D. Bowden, F. M. Hoffman, and R. F. Reynolds (2012), Photoperiodic regulation of the seasonal pattern of photosynthetic capacity and the implications for carbon cycling, *Proceedings of the National Academy of Sciences of the United States of America*, *109*(22), 8612–8617, doi:10.1073/pnas.1119131109/-/DCSupplemental.www.pnas.org/cgi/doi/10.1073/pnas.1119131109.

Behrenfeld, M. J. et al. (2001), Biospheric primary production during an ENSO transition, *Science*, *291*(5513), 2594–7, doi:10.1126/science.1055071.

Bonan, G. (2008a), *Ecological Climatology: Concepts and Applications*, 2nd ed., Cambridge University Press, Cambridge, UK.

Bonan, G. B. (2008b), Forests and climate change: forcings, feedbacks, and the climate benefits of forests, *Science*, *320*, 1444–1449, doi:10.1126/science.1155121.

Brown, M. E., and K. M. de Beurs (2008), Evaluation of multi-sensor semi-arid crop season parameters based on NDVI and rainfall, *Remote Sensing of Environment*, *112*(5), 2261–2271, doi:10.1016/j.rse.2007.10.008.

Brown, M. E., K. de Beurs, and A. Vrieling (2010), The response of African land surface phenology to large scale climate oscillations, *Remote Sensing of Environment*, *114*(10), 2286–2296, doi:10.1016/j.rse.2010.05.005.

Buermann, W., B. Anderson, C. J. Tucker, R. E. Dickinson, W. Lucht, C. S. Potter, and R. B. Myneni (2003), Interannual covariability in Northern Hemisphere air temperatures and greenness associated with El Niño-Southern Oscillation and the Arctic Oscillation, *Journal of Geophysical Research*, *108*, doi:10.1029/2002JD002630.

Chesson, P., R. L. E. Gebauer, S. Schwinning, N. Huntly, K. Wiegand, M. S. K. Ernest, A. Sher, A. Novoplansky, and J. F. Weltzin (2004), Resource pulses, species interactions, and diversity maintenance in arid and semi-arid environments, *Oecologia*, *141*(2), 236–53, doi:10.1007/s00442-004-1551-1.

Cleland, E. E., J. M. Allen, T. M. Crimmins, J. A. Dunne, S. Pau, S. E. Travers, E. S. Zavaleta, and E. M. Wolkovich (2012), Phenological tracking enables positive species responses to climate change, *Ecology*, *93*(8), 1765–1771.

Cobb, K. M., N. Westphal, H. R. Sayani, J. T. Watson, E. Di Lorenzo, H. Cheng, R. L. Edwards, and C. D. Charles (2013), Highly Variable El Nino-Southern Oscillation Throughout the Holocene, *Science*, *339*, 67–70, doi:10.1126/science.1228246.

Cohen, W. B., and S. N. Goward (2004), Landsat's role in ecological applications of remote sensing, *BioScience*, *55*(6), 535–545.

Daly, C., W. P. Gibson, G. H. Taylor, G. L. Johnson, and P. Pasteris (2002), A knowledge-based approach to the statistical mapping of climate, *Climate Research*, *22*, 99–113.

Daly, C., M. Halbleib, J. I. Smith, W. P. Gibson, M. K. Doggett, G. H. Taylor, J. Curtis, and P. P. Pasteris (2008), Physiographically sensitive mapping of climatological temperature and precipitation across the conterminous United States, *International Journal of Climatology*, *28*, 2031–2064, doi:10.1002/joc.

Field, C. B., J. T. Randerson, and C. M. Malmström (1995), Global net primary production: combining ecology and remote sensing, *Remote Sensing of Environment*, *88*, 74–88.

Fisher, J., J. Mustard, and M. Vadeboncoeur (2006), Green leaf phenology at Landsat resolution: Scaling from the field to the satellite, *Remote Sensing of Environment*, *100*(2), 265–279, doi:10.1016/j.rse.2005.10.022.

Fisher, J. I., and J. F. Mustard (2007), Cross-scalar satellite phenology from ground, Landsat, and MODIS data, *Remote Sensing of Environment*, *109*(3), 261–273, doi:10.1016/j.rse.2007.01.004.

Fridley, J. D. (2012), Extended leaf phenology and the autumn niche in deciduous forest invasions, *Nature*, *485*(7398), 359–362, doi:10.1038/nature11056.

Friedl, M. A. et al. (2002), Global land cover mapping from MODIS: algorithms and early results, *Remote Sensing of Environment*, *83*(1-2), 287–302, doi:10.1016/S0034-4257(02)00078-0.

Friedl, M. A., D. Sulla-Menashe, B. Tan, A. Schneider, N. Ramankutty, A. Sibley, and X. Huang (2010), MODIS Collection 5 global land cover: Algorithm refinements and characterization of new datasets, *Remote Sensing of Environment*, *114*(1), 168–182, doi:10.1016/j.rse.2009.08.016.

Ganguly, S., M. A. Friedl, B. Tan, X. Zhang, and M. Verma (2010), Land surface phenology from MODIS: Characterization of the Collection 5 global land cover dynamics product, *Remote Sensing of Environment*, *114*(8), 1805–1816, doi:10.1016/j.rse.2010.04.005.

Goldstein, A. H., N. E. Hultman, J. M. Fracheboud, M. R. Bauer, J. A. Panek, M. Xu, Y. Qi, A. B. Guenther, and W. Baugh (2000), Effects of climate variability on the carbon dioxide, water, and sensible heat fluxes above a ponderosa pine plantation in the Sierra Nevada (CA), *Agricultural and Forest Meteorology*, *101*(2-3), 113–129, doi:10.1016/S0168-1923(99)00168-9.

Gray, J., and C. Song (2012), Mapping leaf area index using spatial, spectral, and temporal information from multiple sensors, *Remote Sensing of Environment*, *119*, 173–183, doi:10.1016/j.rse.2011.12.016.

Hansen, M. C., R. S. DeFries, J. R. G. Townshend, and R. Sohlberg (2000), Global land cover classification at 1 km spatial resolution using a classification tree approach, *International Journal of Remote Sensing*, *21*(6 & 7), 1331–1364.

Hashimoto, H., R. R. Nemani, M. A. White, W. M. Jolly, S. C. Piper, C. D. Keeling, R. B. Myneni, and S. W. Running (2004), El Niño–Southern Oscillation-induced variability in terrestrial carbon cycling, *Journal of Geophysical Research*, *109*, doi:10.1029/2004JD004959.

Heinsch, F. A. et al. (2006), Evaluation of remote sensing based terrestrial productivity from MODIS using regional tower eddy flux network observations, *IEEE Transactions on Geoscience and Remote Sensing*, *44*(7), 1908–1925, doi:10.1109/TGRS.2005.853936.

Holland, P. W., and R. E. Welsch (1977), Robust regression using iteratively reweighted least-squares, *Communications in Statistics - Theory and Methods*, *6*(9), 813–827.

Huete, A., K. Didan, T. Miura, E. P. Rodriguez, X. Gao, and L. G. Ferreira (2002), Overview of the radiometric and biophysical performance of the MODIS vegetation indices, *Remote Sensing of Environment*, *83*(1-2), 195–213, doi:10.1016/S0034-4257(02)00096-2.

Huete, A. R., H. Q. Liu, K. Batchily, and W. van Leeuwen (1997), A comparison of vegetation indices over a global set of TM images for EOS-MODIS, *Remote Sensing of Environment*, *59*, 440–451.

Hwang, T., C. Song, J. M. Vose, and L. E. Band (2011), Topography-mediated controls on local vegetation phenology estimated from MODIS vegetation index, *Landscape Ecology*, *26*(4), 541–556, doi:10.1007/s10980-011-9580-8.

Jolly, W. M., and S. W. Running (2004), Effects of precipitation and soil water potential on drought deciduous phenology in the Kalahari, *Global Change Biology*, *10*, 303–308, doi:10.1046/j.1529-8817.2003.00701.x.

Jolly, W. M., R. Nemani, and S. W. Running (2005), A generalized, bioclimatic index to predict foliar phenology in response to climate, *Global Change Biology*, *11*(4), 619–632, doi:10.1111/j.1365-2486.2005.00930.x.

Jönsson, P., and L. Eklundh (2004), TIMESAT—a program for analyzing time-series of satellite sensor data, *Computers & Geosciences*, *30*(8), 833–845, doi:10.1016/j.cageo.2004.05.006.

Justice, C. O., J. R. G. Townshend, B. N. Holben, and C. J. Tucker (1985), Analysis of the phenology of global vegetation using meteorological satellite data, *International Journal of Remote Sensing*, *6*(8), 1271–1318.

Justice, C. O. et al. (1998), The Moderate Resolution Imaging Spectroradiometer (MODIS): land remote sensing for global change research, *IEEE Transactions on Geoscience and Remote Sensing*, *36*(4), 1228–1249, doi:10.1109/36.701075.

Keeling, C. D., J. F. S. Chin, and T. P. Whorf (1996), Increased activity of northern vegetation inferred from atmospheric CO2 measurements, *Nature*, *382*, 146–149.

Körner, C., and D. Basler (2010), Phenology under global warming, *Science*, *327*(5972), 1461–2, doi:10.1126/science.1186473.

Law, B. E., D. Turner, J. Campbell, O. J. Sun, S. Van Tuyl, W. D. Ritts, and W. B. Cohen (2004), Disturbance and climate effects on carbon stocks and fluxes across Western Oregon USA, *Global Change Biology*, *10*(9), 1429–1444, doi:10.1111/j.1365-2486.2004.00822.x.

Liu, Y., P. B. Reich, G. Li, and S. Sun (2011), Shifting phenology and abundance under experimental warming alters trophic relationships and plant reproductive capacity, *Ecology*, *92*(6), 1201–1207.

Loveland, T. R., B. C. Reed, J. F. Brown, D. O. Ohlen, Z. Zhu, L. Yang, and J. W. Merchant (2000), Development of a global land cover characteristics database and IGBP DISCover from 1 km AVHRR data, *International Journal of Remote Sensing*, *21*(6 & 7), 1303–1330.

Ma, S., D. D. Baldocchi, L. Xu, and T. Hehn (2007), Inter-annual variability in carbon dioxide exchange of an oak/grass savanna and open grassland in California, *Agricultural and Forest Meteorology*, *147*(3-4), 157–171, doi:10.1016/j.agrformet.2007.07.008.

McCabe, G. J., T. R. Ault, B. I. Cook, J. L. Betancourt, and M. D. Schwartz (2012), Influences of the El Niño Southern Oscillation and the Pacific Decadal Oscillation on the timing of the North American spring, *International Journal of Climatology*, *32*, 2301–2310, doi:10.1002/joc.3400.

McPhaden, M. J., S. E. Zebiak, and M. H. Glantz (2006), ENSO as an integrating concept in earth science., *Science*, *314*(5806), 1740–5, doi:10.1126/science.1132588.

Moody, A., and D. M. Johnson (2001), Land-Surface Phenologies from AVHRR Using the Discrete Fourier Transform, *Remote Sensing of Environment*, *75*(3), 305–323, doi:10.1016/S0034-4257(00)00175-9.

Morisette, J. T. et al. (2009), Tracking the rhythm of the seasons in the face of global change: phenological research in the 21st century, *Frontiers in Ecology and the Environment*, *7*(5), 253–260, doi:10.1890/070217.

Moulin, S., L. Kergoat, N. Viovy, and G. Dedieu (1997), Global-scale assessment of vegetation phenology using NOAA/AVHRR satellite measurements, *Journal of Climate*, *10*, 1154–1170.

Mu, Q., M. Zhao, F. A. Heinsch, M. Liu, H. Tian, and S. W. Running (2007), Evaluating water stress controls on primary production in biogeochemical and remote sensing based models, *Journal of Geophysical Research*, *112*(G1), 1–13, doi:10.1029/2006JG000179.

Nemani, R. R., C. D. Keeling, H. Hashimoto, W. M. Jolly, S. C. Piper, C. J. Tucker, R. B. Myneni, and S. W. Running (2003), Climate-driven increases in global terrestrial net primary production from 1982 to 1999, *Science*, *300*(5625), 1560–1563.

Newman, M., S.-I. Shin, and M. a. Alexander (2011), Natural variation in ENSO flavors, *Geophysical Research Letters*, *38*, doi:10.1029/2011GL047658.

Peñuelas, J., T. Rutishauser, and I. Filella (2009), Phenology feedbacks on climate change, *Science*, *324*(5929), 887–8, doi:10.1126/science.1173004.

Potter, C., S. Klooster, R. Myneni, V. Genovese, P.-N. Tan, and V. Kumar (2003a), Continental-scale comparisons of terrestrial carbon sinks estimated from satellite data and ecosystem modeling 1982–1998, *Global and Planetary Change*, *39*(3-4), 201–213, doi:10.1016/j.gloplacha.2003.07.001.

Potter, C., S. Klooster, M. Steinbach, P. Tan, V. Kumar, S. Shekhar, R. Nemani, and R. Myneni (2003b), Global teleconnections of climate to terrestrial carbon flux, *Journal of Geophysical Research*, *108*(D17), 4556, doi:10.1029/2002JD002979.

Potter, C., S. Klooster, M. Steinbach, P.-N. Tan, V. Kumar, S. Shekhar, and C. R. De Carvalho (2004), Understanding global teleconnections of climate to regional model estimates of Amazon ecosystem carbon fluxes, *Global Change Biology*, *10*(5), 693–703, doi:10.1111/j.1529-8817.2003.00752.x.

Potter, C. S., J. T. Randerson, C. B. Field, P. A. Matson, P. M. Vitousek, H. A. Mooney, and S. A. Klooster (1993), Terrestrial ecosystem production: a process model based on global satellite and surface data, *Global Biogeochemical Cycles*, *7*(4), 811–841.

Prince, S., and S. Goward (1995), Global primary production: a remote sensing approach, *Journal of Biogeography*, *22*(4), 815–835.

Rahman, A. F., D. A. Sims, V. D. Cordova, and B. Z. El-Masri (2005), Potential of MODIS EVI and surface temperature for directly estimating per-pixel ecosystem C fluxes, *Geophysical Research Letters*, *32*(L19404), doi:10.1029/2005GL024127.

Redmond, K. T., and R. W. Koch (1991), Surface climate and streamflow variability in the western United States and their relationship to large-scale circulation indices, *Water Resources Research*, *27*(9), 2381–2399.

Reed, B. C., J. F. Brown, D. VanderZee, T. R. Loveland, W. Merchant, and D. O. Ohlen (1994), Measuring Phenological Variability from Satellite Imagery, *Journal of Vegetation Science*, *5*(5), 703–714.

Richardson, A. D. et al. (2010), Influence of spring and autumn phenological transitions on forest ecosystem productivity, *Philosophical Transactions of the Royal Society B: Biological Sciences*, *365*(1555), 3227–46, doi:10.1098/rstb.2010.0102.

Richardson, A. D., T. F. Keenan, M. Migliavacca, Y. Ryu, O. Sonnentag, and M. Toomey (2013), Climate change, phenology, and phenological control of vegetation feedbacks to the climate system, *Agricultural and Forest Meteorology*, *169*, 156–173, doi:10.1016/j.agrformet.2012.09.012.

Running, S. W. (2012), A Measurable Planetary Boundary for the Biosphere, *Science*, *337*, 1458–1459, doi:10.1126/science.1227620.

Running, S. W. et al. (1994), Terrestrial remote sensing science and algorithms planned for EOS/MODIS, *International Journal of Remote Sensing*, *15*(17), 3587–3620.

Running, S. W., R. R. Nemani, F. A. Heinsch, M. Zhao, M. Reeves, and H. Hashimoto (2004), A Continuous Satellite-Derived Measure of Global Terrestrial Primary

Production, *BioScience*, *54*(6), 547–560, doi:10.1641/0006-3568(2004)054[0547:ACSMOG]2.0.CO;2.

Schaaf, C. B. et al. (2002), First operational BRDF, albedo nadir reflectance products from MODIS, *Remote Sensing of Environment*, *83*, 135–148, doi:10.1016/S0034-4257(02)00091-3.

Schwartz, M. D. (1992), Phenology and springtime surface-layer change, *Monthly weather review*, *120*, 2570–2578.

Scott, R. L., G. D. Jenerette, D. L. Potts, and T. E. Huxman (2009), Effects of seasonal drought on net carbon dioxide exchange from a woody-plant-encroached semiarid grassland, *Journal of Geophysical Research*, *114*, G04004, doi:10.1029/2008JG000900.

Scott, R. L., E. P. Hamerlynck, G. D. Jenerette, M. S. Moran, and G. A. Barron-Gafford (2010), Carbon dioxide exchange in a semidesert grassland through drought-induced vegetation change, *Journal of Geophysical Research*, *115*, G03026, doi:10.1029/2010JG001348.

Sims, D. A. et al. (2006a), On the use of MODIS EVI to assess gross primary productivity of North American ecosystems, *Journal of Geophysical Research*, *111*(G4), 1–16, doi:10.1029/2006JG000162.

Sims, D. A., H. Luo, S. Hastings, W. C. Oechel, A. F. Rahman, and J. A. Gamon (2006b), Parallel adjustments in vegetation greenness and ecosystem CO2 exchange in response to drought in a Southern California chaparral ecosystem, *Remote Sensing of Environment*, *103*(3), 289–303, doi:10.1016/j.rse.2005.01.020.

Sims, D. A. et al. (2008), A new model of gross primary productivity for North American ecosystems based solely on the enhanced vegetation index and land surface temperature from MODIS, *Remote Sensing of Environment*, *112*, 1633–1646, doi:10.1016/j.rse.2007.08.004.

Stenseth, N. C., G. Ottersen, J. W. Hurrell, A. Mysterud, M. Lima, K.-S. Chan, N. G. Yoccoz, and B. Adlandsvik (2003), Studying climate effects on ecology through the use of climate indices: the North Atlantic Oscillation, El Niño Southern Oscillation and beyond, *Proceedings of the Royal Society B*, *270*(1529), 2087–96, doi:10.1098/rspb.2003.2415.

Trenberth, K. E. (1997a), Short-term climate variations: Recent accomplishments and issues for future progress, *Bulletin of the American Meteorological Society*, *78*(6), 1081–1096.

Trenberth, K. E. (1997b), The definition of El Niño, *Bulletin of the American Meteorological Society*, *78*(12), 2771–2777.

Trenberth, K. E., and D. P. Stepaniak (2001), Indices of El Niño evolution, *Journal of Climate*, *14*, 1697–1701.

Tucker, C. J. (1979), Red and photographic infrared linear combinations for monitoring vegetation, *Remote sensing of Environment*, *8*(2), 127–150.

Tucker, C. J., J. R. Townshend, and T. E. Goff (1985), African land-cover classification using satellite data, *Science*, *227*(4685), 369–75, doi:10.1126/science.227.4685.369.

Turner, D. P., W. D. Ritts, W. B. Cohen, S. T. Gower, M. Zhao, S. W. Running, S. C. Wofsy, S. Urbanski, A. L. Dunn, and J. W. Munger (2003), Scaling Gross Primary Production (GPP) over boreal and deciduous forest landscapes in support of MODIS GPP product validation, *Remote Sensing of Environment*, *88*(3), 256–270, doi:10.1016/j.rse.2003.06.005.

Turner, D. P. et al. (2006), Evaluation of MODIS NPP and GPP products across multiple biomes, *Remote Sensing of Environment*, *102*(3-4), 282–292, doi:10.1016/j.rse.2006.02.017.

Vecchi, G. A., A. Clement, and B. J. Soden (2008), Examining the Tropical Pacific's Response to Global Warming, *Eos, Transactions American Geophysical Union*, *89*(9), 81–83, doi:10.1029/2008EO090002.

Vicente-Serrano, S. M., N. Delbart, T. Le Toan, and M. Grippa (2006), El Niño–Southern Oscillation influences on the interannual variability of leaf appearance dates in central Siberia, *Geophysical Research Letters*, *33*, L03707, doi:10.1029/2005GL025000.

Viovy, N., O. Arino, and A. S. Belward (1992), The Best Index Slope Extraction (BISE): A method for reducing noise in NDVI time-series, *International Journal of Remote Sensing*, *13*(8), 1585–1590.

White, M. A., P. E. Thornton, and S. W. Running (1997), A continental phenology model for monitoring vegetation responses to interannual climatic variability, *Global Biogeochemical Cycles*, *11*(2), 217–234, doi:10.1029/97GB00330.

White, M. A. et al. (2009), Intercomparison, interpretation, and assessment of spring phenology in North America estimated from remote sensing for 1982-2006, *Global Change Biology*, *15*(10), 2335–2359, doi:10.1111/j.1365-2486.2009.01910.x.

Willis, C. G., B. Ruhfel, R. B. Primack, A. J. Miller-Rushing, and C. C. Davis (2008), Phylogenetic patterns of species loss in Thoreau's woods are driven by climate change., *Proceedings of the National Academy of Sciences of the United States of America*, *105*(44), 17029–17033, doi:10.1073/pnas.0806446105.

Willis, C. G., B. R. Ruhfel, R. B. Primack, A. J. Miller-Rushing, J. B. Losos, and C. C. Davis (2010), Favorable climate change response explains non-native species' success in Thoreau's woods., *PloS one*, *5*(1), e8878, doi:10.1371/journal.pone.0008878.

Wise, E. K. (2010), Spatiotemporal variability of the precipitation dipole transition zone in the western United States, *Geophysical Research Letters*, *37*, L07706, doi:10.1029/2009GL042193.

Wolkovich, E. M., and E. E. Cleland (2011), The phenology of plant invasions: a community ecology perspective, *Frontiers in Ecology and the Environment*, *9*(5), 287–294, doi:10.1890/100033.

Xiao, X., B. Braswell, Q. Zhang, S. Boles, S. Frolking, and B. Moore, III (2003), Sensitivity of vegetation indices to atmospheric aerosols: continental-scale observations in Northern Asia, *Remote Sensing of Environment*, *84*, 385–392.

Yeh, S.-W., J.-S. Kug, B. Dewitte, M.-H. Kwon, B. P. Kirtman, and F.-F. Jin (2009), El Niño in a changing climate, *Nature*, *461*, 511–514, doi:10.1038/nature08316.

Yeh, S.-W., B. P. Kirtman, J.-S. Kug, W. Park, and M. Latif (2011), Natural variability of the central Pacific El Niño event on multi-centennial timescales, *Geophysical Research Letters*, *38*, L02704, doi:10.1029/2010GL045886.

Zhang, X., M. A. Friedl, C. B. Schaaf, A. H. Strahler, J. C. F. Hodges, F. Gao, B. C. Reed, and A. Huete (2003), Monitoring vegetation phenology using MODIS, *Remote Sensing of Environment*, *84*(3), 471–475, doi:10.1016/S0034-4257(02)00135-9.

Zhang, X., M. A. Friedl, and C. B. Schaaf (2006), Global vegetation phenology from Moderate Resolution Imaging Spectroradiometer (MODIS): Evaluation of global patterns and comparison with in situ measurements, *Journal of Geophysical Research*, *111*(G4), 1–14, doi:10.1029/2006JG000217.

Zhang, X., D. Tarpley, and J. T. Sullivan (2007), Diverse responses of vegetation phenology to a warming climate, *Geophysical Research Letters*, *34*(19), 0–4, doi:10.1029/2007GL031447.

Zhang, X., M. A. Friedl, and C. B. Schaaf (2009), Sensitivity of vegetation phenology detection to the temporal resolution of satellite data, *International Journal of Remote Sensing*, *30*(8), 2061–2074, doi:10.1080/01431160802549237.